

Hubble Tension as an Effect of Horizon Entanglement Nonequilibrium

Alexander S. Sakharov  ^{1, 2, *} Rostislav Konoplich  ^{1, 3, †} Merab Gogberashvili  ^{4, 5, ‡} and Jack Simoni  ^{1, §}

¹*Department of Mathematics and Physics, Manhattan University,
4513 Manhattan College Parkway, Riverdale, NY 10471, United States of America*

²*Experimental Physics Department, CERN, CH-1211 Genève 23, Switzerland*

³*Department of Physics, New York University,
726 Broadway, New York, NY 10003, United States of America*

⁴*Department of Exact and Natural Sciences, Javakhishvili Tbilisi State University, Tbilisi 0179, Georgia*

⁵*Department of High Energy Physics, Andronikashvili Institute of Physics, Tbilisi 0177, Georgia*

(Dated: January 27, 2026)

We propose an infrared mechanism for alleviating the Hubble constant tension, based on a small departure from entanglement equilibrium at the cosmological apparent horizon. If the horizon entanglement entropy falls slightly below the Bekenstein–Hawking value, we parametrize the shortfall by a fractional deficit $\delta(a)$ evolving with the FLRW scale factor a . The associated equipartition deficit at the Gibbons–Hawking temperature then sources a smooth, homogeneous component whose density scales as H^2/G , with a dimensionless coefficient $c_e^2(a)$ of order unity times $\delta(a)$. Because this component tracks H^2 , it is negligible at early times but can activate at redshifts $z \lesssim 1$, raising the late time expansion rate by a few percent without affecting recombination or the sound horizon. We present a minimal three parameter activation model for $c_e^2(a)$ and derive its impact on the background expansion, effective equation of state, and linear growth for a smooth entanglement sector. The framework predicts a small boost in $H(z)$, a mild suppression of $f\sigma_8(z)$, and a corresponding modification of the low- z distance–redshift relation. We test these predictions against current low-redshift data sets, including SN Ia distance moduli, baryon acoustic oscillation distance measurements, cosmic chronometer $H(z)$ data, and redshift space distortion constraints, and discuss whether the H_0 tension can be consistently interpreted as a late-time, horizon-scale information deficit rather than an early universe modification.

I. INTRODUCTION

A persistent discrepancy has emerged between the Hubble constant inferred from early universe probes and the value obtained from late-time distance ladders, a percent level tension that, if not due to unrecognized systematics, hints at new physics in the cosmic expansion history. Concretely, the CMB anisotropy spectrum tightly constrains the angular acoustic scale and, within a specified background model, translates this into an inferred H_0 through the sound horizon and the late-time distance to last scattering. For example, *Planck* 2018 (under Λ CDM) finds $H_0 = 67.4 \pm 0.5 \text{ km s}^{-1} \text{ Mpc}^{-1}$ [1], whereas local distance ladder calibrations anchored by geometric and stellar standardization methods yield higher values; in particular, SH0ES reports $H_0 = 73.30 \pm 1.04 \text{ km s}^{-1} \text{ Mpc}^{-1}$ [2]. At intermediate redshifts, baryon acoustic oscillations (BAO) provide a robust standard ruler that strongly constrains the late-time distance–redshift relation; recent DESI BAO constraints favor values closer to the *Planck* inferred scale [3, 4], sharpening the question of whether a consistent cosmological history can reconcile early- and late-time determinations. Explanations proposed so far broadly fall into two classes. Early time modifications (e.g., early dark energy, extra radiation, or altered recombination) reduce the sound horizon so the CMB can accommodate a larger H_0 , while late-time ideas (e.g., evolving dark energy or modified gravity) adjust the low- z Hubble rate with minimal impact on recombination; see Refs. [5–8] for reviews. Both directions face tight joint constraints from CMB anisotropies, BAO, Type-Ia supernova distances, and structure growth observables: DESI BAO remain consistent with flat Λ CDM and bound w near -1 , Pantheon+ tightens the low- z distance–redshift relation, and redshift distortion (RSD) growth measurements strongly restrict early time solutions such as EDE when combined with CMB data [3, 4, 9–13].

In parallel, advances in quantum information and gravity have reshaped how we think about spacetime: horizons carry entropy and temperature; entanglement can encode geometry; and thermodynamic reasoning can reproduce gravitational dynamics. However, naive free-field entanglement in curved spacetime contributes only $\mathcal{O}(H^4)$ to the vacuum energy far too small to matter cosmologically and the ultra violet (UV) area law renormalizes $1/G$ rather than producing a new fluid. Any entanglement driven resolution of the Hubble tension must therefore be infrared (IR) and horizon tied, not a re-counting of UV modes.

We develop and assess such an IR mechanism: the *horizon entanglement equipartition deficit* (HEED). The core hypothesis is that the quantum state of our late time universe is slightly out of entanglement equilibrium at the apparent (Hubble) horizon. If the actual horizon entanglement entropy S_{ent} falls short of the Bekenstein–Hawking value $S_{\text{BH}} = A/(4G)$ by a fractional deficit $\delta(a) \in [0, 1]$, then treating the horizon as an entanglement screen at the Gibbons–Hawking temperature $T_{\text{dS}} = H/(2\pi)$ the resulting equipartition deficit translates into a homogeneous bulk

component of density

$$\rho_{\text{HEED}}(a) = \frac{3}{8\pi G} c_e^2(a) H^2(a), \quad c_e^2(a) \sim \mathcal{O}(1) \times \delta(a), \quad (1)$$

where $H(a)$ stand for the Hubble rate evolving with the FLRW scale factor a . This is the familiar holographic H^2/G [14–17], but with a time-dependent coefficient tied to horizon entanglement rather than an ad hoc constant.

Two features make HEED cosmologically attractive. First, because $\rho_{\text{HEED}} \propto H^2$, it is automatically negligible at high redshift relative to matter and radiation, preserving recombination physics and the sound horizon. Second, a late time activation $c_e^2(a) = c_{e0}^2 g(a)$ with a smooth switch, $g(a, a_t, k)$ at scale factor a_t characterized by steepness k , naturally yields a few percent increase in the low- z Hubble rate, sufficient to ease the tension while remaining consistent with SN/BAO distances. Interpreted as a smooth, non-clustering sector (rest frame sound speed $\simeq 1$), HEED modestly suppresses structure growth as probed by $f\sigma_8$ and generically increases the late integrated Sachs–Wolfe (ISW) signal, i.e. the large scale CMB temperature anisotropy sourced by the late-time decay of gravitational potentials. Although ISW measurements are not considered in the present study, this effect offers an additional, in-principle observable lever for distinguishing HEED from purely geometric modifications.

Two features make HEED cosmologically attractive. First, because $\rho_{\text{HEED}} \propto H^2$, it is automatically negligible at high redshift relative to matter and radiation, thereby preserving recombination physics and the sound horizon. Second, we model a *late-time activation* of the HEED amplitude by letting

$$c_e^2(a) = c_{e0}^2 g(a; a_t, k), \quad (2)$$

where the dimensionless switch function $g(a; a_t, k)$ interpolates smoothly from $g \ll 1$ at early times ($a \ll a_t$) to $g \rightarrow 1$ at late times ($a \gtrsim a_t$). The parameter a_t sets the characteristic activation epoch (equivalently $z_t \simeq a_t^{-1} - 1$), while k controls the sharpness of the transition (larger k corresponds to a steeper switch). This late activation can yield a few percent increase in the low- z Hubble rate, sufficient to ease the tension while remaining consistent with SN/BAO distances. Interpreted as a smooth, non-clustering sector (rest-frame sound speed $\simeq 1$), HEED modestly suppresses structure growth through $f\sigma_8$, providing an additional levers beyond purely geometric constraints.

Conceptually, HEED can be read in two equivalent ways. In a *fluid* picture, ρ_{HEED} adds to the stress–energy budget and the Friedmann equation becomes

$$H^2(a) = \frac{8\pi G}{3} \frac{\rho_m(a) + \rho_\Lambda}{1 - c_e^2(a)}, \quad (3)$$

where $\rho_m(a) = \rho_{m0} a^{-3}$ is the (pressureless) matter density and $\rho_\Lambda \equiv \Lambda/(8\pi G)$ is the vacuum energy density associated with the cosmological constant. The entanglement deficit therefore appears as a multiplicative correction to the expansion rate. In a *modified gravity* reading, the same factor reshapes the effective Planck mass, $M_*^2(a) = M_{\text{Pl}}^2 [1 - c_e^2(a)]$, while matter remains covariantly conserved. Either view preserves the Bianchi identity and avoids ghost/gradient instabilities so long as the entanglement sector is treated as smooth and non-propagating (an effective IR dressing of the background rather than a new field).

This paper makes following contributions. We formalize HEED from horizon thermodynamics and entanglement equilibrium, clarifying the UV/IR split: UV area law pieces renormalize $1/G$, whereas the IR deficit $\delta(a)$ sources $\rho \propto H^2/G$. We derive background relations closed form, an instantaneous effective $w_{\text{HEED}}(a)$, and the logarithmic derivative $d \ln H / d \ln a$ needed for growth under a minimal three parameter activation $\{c_{e0}^2, a_t, k\}$. We analyze linear perturbations with a smooth entanglement sector, predicting a characteristic pattern: small late time boosts to $H(z)$ and mild suppression of $f\sigma_8$. We confront the model with low-redshift data by fitting SN Ia, BAO, and cosmic chronometer (CC) constraints together with a CMB distance prior that keeps the sound horizon fixed, and by testing the resulting growth history against RSD measurements, while imposing the early-time safety condition $c_e^2(a_*) \ll 1$ at recombination.

HEED sits at the intersection of holographic dark energy type scalings and entanglement equilibrium thinking. Unlike standard HDE with a constant c^2 , HEED explains the coefficient as a dynamical horizon information shortfall that can switch on at $z \lesssim 1$. Unlike free field “entanglement dark energy,” it avoids the $\mathcal{O}(H^4)$ suppression by tying directly to the horizon’s IR thermodynamics.

The paper is organized as follows. Section II derives HEED from horizon thermodynamics and entanglement considerations, establishes the characteristic H^2/G scaling, and clarifies the required UV/IR separation; it also presents the background dynamics, the instantaneous effective equation of state, and the minimal activation parameterization. Section III confronts the HEED activation parameters with a combination of four low- z probes. The Bayesian inference framework is described in Sec. III A, where the posterior is sampled with the affine-invariant ensemble sampler `emcee`. Marginalized constraints and triangle plots are obtained with `GetDist` and interpreted in Sec. III B, which discusses posterior constraints and the internal consistency of the HEED picture. Section IV summarizes the main results and outlines directions for future work.

II. HORIZON ENTANGLEMENT EQUIPARTITION DEFICIT

The HEED framework starts from the observation that, in a spatially flat FLRW universe, the apparent (Hubble) horizon behaves thermodynamically: it has a well-defined area and an associated temperature and entropy, in direct analogy with de Sitter and black hole horizons [18–21]. We posit that the *renormalized* bulk entanglement entropy of quantum fields across this horizon is slightly below the Bekenstein–Hawking value [18–21]. This small shortfall, which we call “entanglement deficit”, encodes a departure from entanglement equilibrium and, when translated through horizon equipartition [22–25], manifests as an infrared, horizon tied contribution to the cosmic energy budget whose magnitude tracks the square of the expansion rate as H^2/G . Because this contribution is naturally tiny at early times and only becomes relevant as the universe accelerates, it can modify the late time expansion without upsetting recombination physics, unlike free field vacuum effects whose influence scales much more weakly with the Hubble rate (see Appendix A for details).

Let Σ_H denote the apparent (Hubble) horizon on a constant time FLRW slice, and decompose the Cauchy slice into an inside region \mathcal{R}_{in} bounded by Σ_H and its complement \mathcal{R}_{out} . In a QFT without gauge constraints one may (formally) factorize the Hilbert space as $\mathcal{H} \simeq \mathcal{H}_{\text{in}} \otimes \mathcal{H}_{\text{out}}$; with gauge or gravitational constraints it is cleaner to work with local operator algebras (possibly with a shared center or edge modes on Σ_H) that reproduce the usual reduced-state construction [26–28]. The global (total) state ρ_{tot} is a positive, unit-trace operator on the full Hilbert space, $\text{Tr } \rho_{\text{tot}} = 1$. Tracing out exterior degrees of freedom defines the reduced inside state

$$\rho_{\text{in}}(a) \equiv \text{Tr}_{\text{out}} \rho_{\text{tot}}(a), \quad (4)$$

and the entanglement entropy across Σ_H is

$$S_{\text{ent}}(a) = -\text{Tr}_{\text{in}} \rho_{\text{in}}(a) \ln \rho_{\text{in}}(a). \quad (5)$$

As in flat space, vacuum entanglement entropy across a smooth surface exhibits an area–law divergence [26, 29, 30],

$$S_{\text{ent}}^{\text{bare}} = \eta \frac{A(\Sigma_H)}{\epsilon^2} + \dots, \quad (6)$$

with nonuniversal coefficient η and cutoff ϵ . In semiclassical gravity, the same UV modes that produce the area term renormalize the Einstein–Hilbert coupling, so the generalized entropy relevant for horizon thermodynamics reads

$$S_{\text{gen}}[\Sigma_H] = \frac{A(\Sigma_H)}{4G_{\text{ren}}} + S_{\text{bulk}}^{\text{ren}}[\Sigma_H] + \dots, \quad (7)$$

where the divergence has been absorbed into G_{ren} and $S_{\text{bulk}}^{\text{ren}}$ is the finite, IR renormalized bulk entropy term associated with quantum fields across Σ_H [31–34]. In what follows, $S_{\text{ent}}(a)$ denotes this renormalized IR contribution,

$$S_{\text{ent}}(a) \equiv S_{\text{bulk}}^{\text{ren}}[\Sigma_H(a)], \quad (8)$$

which we compare to the Bekenstein–Hawking value $S_{\text{BH}} = A(\Sigma_H)/(4G_{\text{ren}})$. Departures from entanglement equilibrium are then captured by the fractional deficit

$$\delta(a) \equiv 1 - \frac{S_{\text{ent}}(a)}{S_{\text{BH}}(a)} \in [0, 1], \quad (9)$$

with $\delta = 0$ expected in exact de Sitter and $\delta > 0$ natural out of equilibrium at late times [35, 36]. Using the apparent horizon temperature $T_{\text{dS}} = H/(2\pi)$ [18], we will map this deficit to a smooth IR component scaling as H^2/G .

To construct the HEED term, we treat the apparent horizon as an entanglement screen with area and temperature

$$A = \frac{4\pi}{H^2}, \quad T_{\text{dS}} = \frac{H}{2\pi}, \quad (10)$$

and Bekenstein–Hawking entropy $S_{\text{BH}} = A/(4G)$ [18–21]. Calling it an *entanglement screen* means we regard the horizon as the codimension one surface across which we compute the (renormalized) bulk entanglement S_{ent} of quantum fields. The screen then supplies a “bookkeeping device” for associating a surface energy via equipartition to the bulk IR component. This language is in line with horizon thermodynamics, holographic ideas, and (membrane paradigm) coarse graining of horizon dof [22–25, 37, 38].

Following the emergent–gravity/equipartition literature, we count the effective surface degrees of freedom (DoF) as¹

$$N_{\text{surf}} = \frac{A}{L_p^2} = \frac{A}{G} = \frac{4\pi}{G H^2} = 4 S_{\text{BH}}, \quad (11)$$

which follows directly from the area law for S_{BH} [19, 21]. This is a coarse grained count that does not assume a specific microscopic model and is routinely employed in horizon equipartition derivations of gravitational dynamics [22–25]. We then assume equipartition on the screen,

$$E_{\text{surf}} = \frac{1}{2} N_{\text{surf}} T_{\text{dS}}, \quad (12)$$

with de Sitter temperature $T_{\text{dS}} = H/(2\pi)$ [18]. If only a fraction $1 - \delta(a)$ of these DoF are entanglement active, the *missing* (deficit) energy on the screen is

$$\Delta E_{\text{surf}} = \frac{1}{2} \delta(a) N_{\text{surf}} T_{\text{dS}} = \delta(a) \frac{1}{G H}, \quad (13)$$

where the last equality follows from inserting N_{surf} in Eq. (11) and $T_{\text{dS}} = H/(2\pi)$. Associating this with a homogeneous bulk component within the Hubble volume $V_H = \frac{4\pi}{3} H^{-3}$ gives

$$\rho_{\text{HEED}}(a) = \frac{\Delta E_{\text{surf}}}{V_H} = \frac{3}{4\pi} \delta(a) \frac{H^2(a)}{G} = \frac{3}{8\pi G} c_e^2(a) H^2(a), \quad c_e^2(a) \equiv 2 \delta(a), \quad (14)$$

up to an overall numerical convention of order unity. This realizes the familiar holographic H^2/G scaling while anchoring it to IR horizon entanglement rather than to the UV area law, whose divergence renormalizes $1/G$ and therefore does not represent a dynamical fluid [31–33]. Our statement that HEED “anchors” this scaling to IR entanglement means: instead of postulating $\rho \propto H^2$, we derive it from the horizon’s thermodynamics and a finite, IR entanglement deficit $S_{\text{ent}} < S_{\text{BH}}$, via the equipartition argument in the text. By contrast, the UV area law term in S_{ent} is regulator dependent and simply renormalizes $1/G$; it is not a dynamical fluid [31–33]. Thus HEED ties the coefficient to a physical deficit $\delta(a)$, rather than treating c_e^2 as an external constant.

There are two equivalent but conceptually distinct embeddings of Eq. (14) in FLRW. In a fluid (additive) view one writes

$$H^2(a) = \frac{8\pi G}{3} [\rho_m(a) + \rho_\Lambda + \rho_{\text{HEED}}(a)], \quad \rho_{\text{HEED}}(a) = \frac{3}{8\pi G} c_e^2(a) H^2(a), \quad (15)$$

which leads to the relation

$$H^2(a) = \frac{8\pi G}{3} \frac{\rho_m(a) + \rho_\Lambda}{1 - c_e^2(a)}. \quad (16)$$

Alternatively, in a modified–gravity (multiplicative) view, one moves the factor $1 - c_e^2(a)$ to the geometric side and interprets it as a slowly varying Planck mass [39, 40], $M_*^2(a) = M_{\text{Pl}}^2 [1 - c_e^2(a)]$. In either interpretation the Bianchi identity is respected and matter remains covariantly conserved, $\dot{\rho}_m + 3H\rho_m = 0$ ². Early time safety is guaranteed by requiring $c_e^2(a_*) \ll 1$ at recombination so the sound horizon and CMB acoustic physics remain unchanged.

For phenomenology we model a smooth late–time activation as follows,

$$c_e^2(a) = c_{e0}^2 g(a), \quad g(a) = \frac{1 + (a_t/a)^k}{1 + (a_t/a)^k}, \quad g(1) = 1, \quad (17)$$

with $a_t \in [0.4, 0.8]$ and $k \gtrsim 3$. The normalization $g(1) = 1$ makes $c_{e0}^2 = c_e^2(a=1)$ the present day HEED fraction. Equation (16) rescales the Friedman equation by factor

$$Q^2(a) \equiv \frac{H^2(a)}{H_0^2} = \frac{\Omega_m a^{-3} + \Omega_\Lambda}{1 - c_{e0}^2 g(a)}, \quad \Omega_\Lambda = 1 - \Omega_m. \quad (18)$$

¹ The *Planck length* is $L_p \equiv \sqrt{\hbar G/c^3}$; in the natural units used here ($\hbar = c = \kappa = 1$) one has $L_p^2 = G$. It sets the area quantum that appears in black hole horizon thermodynamics [19, 21].

² The twice contracted Bianchi identity $\nabla_\mu G^{\mu\nu} = 0$ is a geometric identity [41, 42]. With Einstein’s equation $G^{\mu\nu} = 8\pi G T^{\mu\nu}$ this implies covariant conservation $\nabla_\mu T^{\mu\nu} = 0$. For a homogeneous fluid component this yields $\dot{\rho} + 3H(\rho + p) = 0$, and for pressureless matter $\dot{\rho}_m + 3H\rho_m = 0$, as used in the text.

An instantaneous effective equation of state for the HEED sector follows from $\rho_{\text{HEED}} \propto H^2 c_e^2$,

$$w_{\text{HEED}}(a) = -1 - \frac{1}{3} \frac{d}{d \ln a} \ln [Q^2(a) c_e^2(a)] = -1 - \frac{1}{3} \left(\frac{d \ln Q^2}{d \ln a} + \frac{d \ln c_e^2}{d \ln a} \right), \quad (19)$$

with

$$\frac{d \ln Q^2}{d \ln a} = \frac{-3 \Omega_m a^{-3}}{\Omega_m a^{-3} + \Omega_\Lambda} + \frac{1}{1 - c_e^2(a)} \frac{dc_e^2(a)}{d \ln a}. \quad (20)$$

Once c_e^2 has saturated ($d \ln c_e^2/d \ln a \simeq 0$), one finds $w_{\text{HEED}} \approx -1 - \frac{1}{3} d \ln Q^2/d \ln a \approx -1 + \Omega_m(a)$, i.e., quintessence like behavior today for $\Omega_{m0} \simeq 0.3$.

During the switch on ($d \ln c_e^2/d \ln a > 0$), a transient $w_{\text{HEED}} < -1$ can occur. This phantom behavior pertains only to the background effective equation of state and, because HEED introduces no propagating field, it does not signal a ghost. A ghost is a propagating mode with a negative kinetic term, which renders the Hamiltonian unbounded. In a canonical single field, achieving $w < -1$ indeed requires the wrong sign kinetic term and is pathological [43], and k -essence generically cannot stably cross $w = -1$ without ghost/gradient problems [44]. By contrast, within the EFT/Horndeski framework one can realize an effective $w_{\text{eff}} < -1$ while remaining ghost free provided the kinetic matrices are positive, the scalar sound speed satisfies $c_s^2 > 0$, and the effective Planck mass remains positive ($M_*^2 > 0$), e.g., in the α -parameterization [39, 40, 45–48]. HEED belongs to this safe class: it is an effective, nonpropagating IR sector equivalent to a mild time variation of $M_*^2(a) = M_{\text{Pl}}^2[1 - c_e^2(a)]$ with $0 \leq c_e^2(a) < 1$, so any transient $w_{\text{HEED}} < -1$ during the switch-on of $c_e^2(a)$ is a kinematic background effect rather than a ghost instability. Taking $\alpha_T = 0$ and $\alpha_B \simeq \alpha_K \simeq 0$ ³ keeps the extra scalar nondynamical while satisfying standard no-ghost/no-gradient conditions [39, 40].

In the HEED framework we treat the entanglement sector as smooth (non-clustering) and work in GR for linear perturbations. The matter growth factor $D(a)$ (normalized so that $D(1) = 1$) obeys the standard ODE

$$D'' + \left[2 + \frac{d \ln H}{d \ln a} \right] D' - \frac{3}{2} \Omega_m(a) D = 0, \quad \Omega_m(a) = \frac{\Omega_m a^{-3}}{Q^2(a)}, \quad (21)$$

with primes denoting $d/d \ln a$ and initial conditions set deep in matter domination⁴. Defining the dimensionless logarithmic growth rate

$$f(a) \equiv \frac{d \ln D}{d \ln a}, \quad (22)$$

and the fluctuation amplitude within $8 h^{-1} \text{Mpc}$ spheres (with $h \equiv H_0/100 \text{ km s}^{-1} \text{ Mpc}^{-1}$ the reduced Hubble constant),

$$\sigma_8(a) \equiv \sigma_{8,0} D(a), \quad (23)$$

the RSD observable is the product $f\sigma_8(z)$ which is robust to linear galaxy bias and widely used to test late time dynamics [51, 52]. For HEED backgrounds,

$$\frac{d \ln H}{d \ln a} = \frac{1}{2} \frac{d \ln Q^2}{d \ln a} = -\frac{3}{2} \Omega_m(a) + \frac{1}{2} \frac{dc_e^2/d \ln a}{1 - c_e^2}, \quad (24)$$

so the “friction” term in Eq. (21) is slightly enhanced during the HEED switch on ($dc_e^2/d \ln a > 0$), yielding a mild suppression of growth relative to ΛCDM at $z \lesssim 1$. Once $c_e^2(a)$ saturates ($dc_e^2/d \ln a \simeq 0$) the growth history closely tracks that of a smooth dark energy model with the same $Q(a)$. A useful approximation for intuition is the growth index form $f(a) \simeq \Omega_m(a)^\gamma$ with $\gamma \simeq 0.55$ in GR and small, $w(a)$ dependent corrections for smooth dark energy [51]. The HEED behaves like such a smooth sector and therefore predicts percent level shifts in $f\sigma_8(z)$ concentrated at low redshift (as illustrated in Fig. 1).

These features have clear observational implications. At $a = 1$, Eq. (18) gives $Q^2(1) = 1/(1 - c_{e0}^2)$, so the inferred Hubble constant is boosted by $H_0^{(\text{eff})}/H_0 = (1 - c_{e0}^2)^{-1/2}$, as illustrated in Fig. 2. A modest $c_{e0}^2 = 0.06$ yields a $\sim 3.1\%$

³ α_T (tensor-speed excess) controls the propagation speed of gravitational waves, $c_T^2 = 1 + \alpha_T$. Low-redshift bounds from GW170817/GRB170817A imply $|\alpha_T| \approx 0$ today [40]. α_B (braiding) quantifies kinetic mixing between the scalar sector and the metric (“kinetic gravity braiding”), modifying the Poisson equation and the metric slip and thus growth/ISW signals [39, 48]. α_K (kineticity) measures the normalization of the scalar perturbation’s kinetic term in unitary gauge; it affects the scalar sound speed and no-ghost/no-gradient stability conditions but does not directly modify the tensor sector [39, 47].

⁴ See, e.g., [49–51] for derivations and discussions of linear growth in GR.

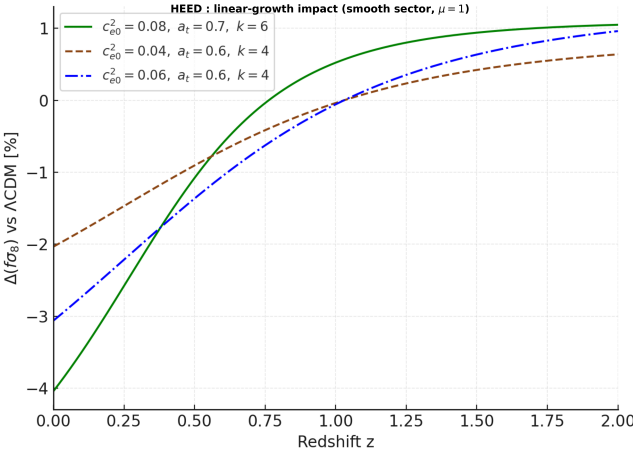


FIG. 1. HEED’s linear growth impact illustrated for three sets of the activation parameters.

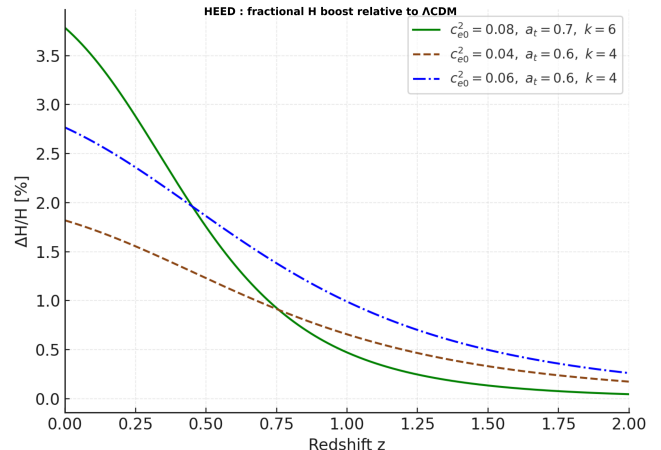


FIG. 2. HEED corrected low redshift Hubble constant related via its residuals relative to the Λ CDM calculations.

increase, while $c_{e0}^2 = 0.10$ gives $\sim 5.3\%$. Because $g(a \ll a_t) \ll 1$, recombination era distances and the sound horizon remain essentially unchanged, providing exactly the lever arm required by the early–late H_0 discrepancy. Low-redshift distance indicators (SN/BAO) can be matched with gentle adjustments driven by the amplitude of c_{e0}^2 and parameters a_t and k describing the activation history. A practical data strategy is to fit SN+BAO+CC backgrounds with a CMB distance prior to keep the sound horizon r_d standard, then test RSD $f\sigma_8(z)$ [52, 53], enforcing the early time prior $c_e^2(a_*) \ll 1$ at recombination.

Finally, we note relationships and distinctions with neighboring ideas. Modular Hamiltonian first law analyses for ball regions show that free or conformal fields produce $\delta\rho \sim H^4$ corrections [54–59] (see Appendix A for details), far too small to be cosmologically relevant; HEED avoids this suppression by tying the effect to IR horizon thermodynamics. Standard holographic dark energy simply posits $\rho \propto H^2/G$ with a constant coefficient; HEED explains that coefficient as a time dependent horizon entanglement shortfall $c_e^2(a) = 2\delta(a)$ with a natural late time activation. The framework is local in time (apparent horizon) and thus avoids teleological issues associated with future event horizons [18, 22, 25, 60]. In sum, HEED constitutes a thermodynamically motivated, IR entanglement mechanism that is internally consistent (conservation, stability, horizon thermodynamics), naturally small at high redshift, and predictive for late time expansion and linear growth [60].

III. OBSERVATIONAL CONSISTENCY ANALYSIS

In this section we confront the HEED activation parameter triplet with a combination of four low- z probes, treated as independent Gaussian constraints. We use SN Ia distance moduli $\mu(z)$ from Pantheon+ [9, 61]; cosmic–chronometer (CC) determinations of $H(z)$ from differential age measurements of passively evolving early-type galaxies [62–68]; compressed BAO measurements of the transverse comoving distance $d_M(z)/r_d$ and the radial comoving Hubble distance $d_H(z)/r_d$ from BOSS DR12 [10], eBOSS DR16 [11] and DESI DR2 [4], adopting a fixed sound horizon r_d [1]; and RSD measurements of the growth rate $f\sigma_8(z)$ from BOSS/eBOSS [10, 69–74], together with WiggleZ [75], VIPERS [76–81], supplemented by very low- z [82–86] and high- z [87–90] constraints.

For the CC sample we employ the community “classic” 31-point set, typically treated as uncorrelated, assembled from DA measurements (see Table I in Appendix B); in this approach the redshift–age relation yields dz/dt , which is converted to the Hubble parameter via $H(z) = -(1+z)^{-1}dz/dt$. The BAO observables used here are compiled from Refs. [4, 10, 11], with the full list of points provided in Table II of Appendix B. Finally, Table III of Appendix B presents a consolidated set of 63 RSD measurements of the linear growth rate, reported as $f\sigma_8(z)$ with 1σ uncertainties and spanning $z \simeq 0.001–1.944$, compiled in Ref. [91]. This compilation includes very low- z peculiar velocity and Tully–Fisher constraints from 2MTF [82], 2MRS [83, 84], and 6dFGS/6dFGS+SNe [85, 86]; early RSD determinations from SDSS–LRG [92] (including the SDSS–LRG–200/60 re-analyses [93]) and DR7–LRG [94]; low- z galaxy–survey results from SDSS–MGS [95], SDSS–veloc [96], DR13 [97], and GAMA [98]; the WiggleZ three-point set [75]; extensive BOSS measurements—LOWZ/CMASS and DR10–DR12 from Refs. [10, 11, 69–74]; multiple VIPERS determinations (including v7 and PDR–2) [76–81]; additional SDSS DR7 peculiar–velocity work [99]; the FastSound high- z constraint [87]; and the SDSS–IV QSO tomographic measurements at $z = 0.978, 1.23, 1.526, 1.944$ [88–90].

Distances follow the standard flat FLRW relations with $H(z)$ defined in Eq. (17) and Eq. (18):

$$d_C(z) = \int_0^z \frac{c dz'}{H(z')}, \quad d_M(z) = d_C(z), \quad d_L(z) = (1+z)d_M(z), \quad \mu(z) = 5 \log_{10}(D_L/\text{Mpc}) + 25. \quad (25)$$

BAO observables are d_M/r_d and d_H/r_d with $d_H \equiv c/H$.

We analyze HEED in the *additive embedding* at the level of the homogeneous background, in which the entanglement sector contributes an algebraic H^2 -proportional term to the Friedmann equation expressed by Eq. (15). Eliminating ρ_{HEED} gives the closed background relation expressed by Eq. (18). We normalize the activation so that $c_e^2(a=1) = c_{e0}^2$, and parameterize

$$c_e^2(a) = c_{e0}^2 g(a), \quad (26)$$

with $g(1) = 1$ and a late-time switch-on controlled by (a_t, k) , as in Eq. (17). In this embedding it is convenient to define the *effective* late-time Hubble scale,

$$H_0^{\text{eff}} \equiv H(a=1) = \frac{H_0}{\sqrt{1 - c_{e0}^2}}, \quad (27)$$

which is the quantity constrained by local measurements. Linear growth assumes a smooth, non-clustering HEED sector in general relativity (GR) so that the growth factor $D(a)$ satisfies Eq. (21) integrated from matter domination with $D(a=1) = 1$. The RSD prediction is

$$f\sigma_8(z) = \frac{d \ln D}{d \ln a} \Big|_{a=1/(1+z)} \sigma_{8,0} D \left(a = \frac{1}{1+z} \right), \quad (28)$$

with $\sigma_{8,0}$ held fixed as a Gaussian prior.

A. Bayesian formulation

The baseline parameter vector in use is

$$\boldsymbol{\theta} = \{H_0, \Omega_m, c_{e0}^2, a_t, k, \sigma_8\}, \quad (29)$$

where H_0 is the underlying Hubble constant entering Eq. (18), while H_0^{eff} is given by Eq. (27). The data vector $\mathbf{d} = \{\boldsymbol{\mu}^{\text{obs}}, \mathbf{b}^{\text{obs}}, \mathbf{h}^{\text{obs}}, \mathbf{g}^{\text{obs}}\}$ collects SNIa distance moduli $\boldsymbol{\mu}^{\text{obs}}$, BAO points $\mathbf{b}^{\text{obs}} \equiv \{D_M/r_d, D_H/r_d\}$, CC measurements $\mathbf{h}^{\text{obs}} \equiv \{H(z)\}$, and RSD growth measurements $\mathbf{g}^{\text{obs}} \equiv \{f\sigma_8(z)\}$. For a given $\boldsymbol{\theta}$, the corresponding predictions $\boldsymbol{\mu}^{\text{th}}(\boldsymbol{\theta})$, $\mathbf{b}^{\text{th}}(\boldsymbol{\theta})$, $\mathbf{h}^{\text{th}}(\boldsymbol{\theta})$, and $\mathbf{g}^{\text{th}}(\boldsymbol{\theta})$ are computed from $H(z; \boldsymbol{\theta})$ via Eqs. (25), (21), and (28).

We define the posterior as

$$\mathcal{P}(\boldsymbol{\theta} \mid \mathbf{d}) \propto \mathcal{L}(\mathbf{d} \mid \boldsymbol{\theta}) \Pi(\boldsymbol{\theta}), \quad \ln \mathcal{L} = -\frac{1}{2} \chi_{\text{tot}}^2(\boldsymbol{\theta}), \quad (30)$$

with the total quadratic statistic

$$\chi_{\text{tot}}^2(\boldsymbol{\theta}) = \chi_{\text{SN}}^2 + \chi_{\text{BAO}}^2 + \chi_{\text{CC}}^2 + \chi_{\text{RSD}}^2 + \chi_{\sigma_8}^2 + \chi_{\text{prior}}^2, \quad (31)$$

assuming Gaussian errors and (for this baseline analysis) independence between data blocks.

The SN term uses Hubble diagram residuals and profiles out a single additive offset ΔM , encoding the absolute magnitude (distance zero-point) degeneracy with the Hubble scale. With diagonal errors the raw statistic is

$$\chi_{\text{SN}}^2(\boldsymbol{\theta}, \Delta M) = \sum_i \frac{[\mu_i - \mu_{\text{th}}(z_i; \boldsymbol{\theta}) - \Delta M]^2}{\sigma_{\mu,i}^2}, \quad (32)$$

where $\mu_{\text{th}}(z)$ is evaluated from $H(z)$. Minimization of Eq. (32) with respect to ΔM yields the analytic profiler

$$\Delta M^*(\boldsymbol{\theta}) = \frac{\sum_i [\mu_i - \mu_{\text{th}}(z_i; \boldsymbol{\theta})]/\sigma_{\mu,i}^2}{\sum_i 1/\sigma_{\mu,i}^2}, \quad \chi_{\text{SN}}^2(\boldsymbol{\theta}) \equiv \chi_{\text{SN}}^2(\boldsymbol{\theta}, \Delta M^*(\boldsymbol{\theta})), \quad (33)$$

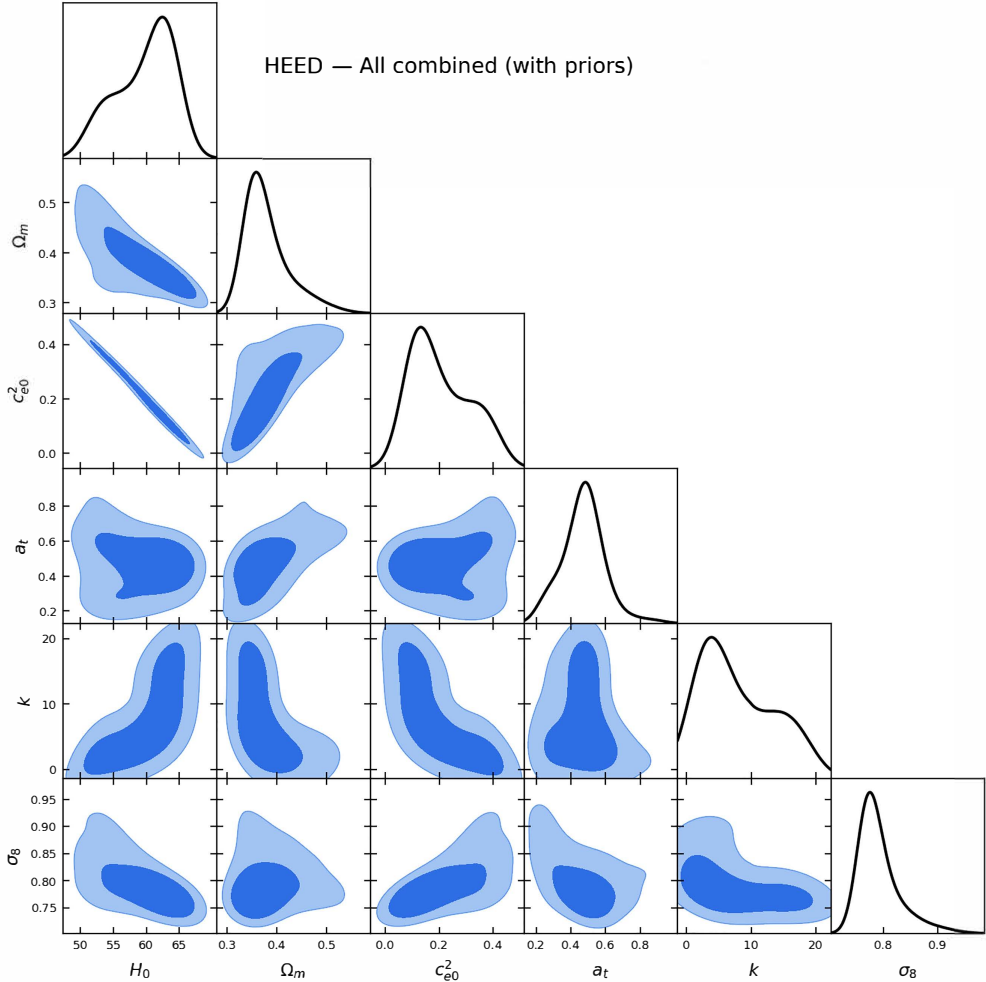


FIG. 3. Triangle plot for the HEED parameterization showing the marginalized posterior distributions of $\{H_0, \Omega_m, c_{e0}^2, a_t, k, \sigma_8\}$ obtained from the joint SN+BAO+CC+RSD likelihood. Shaded contours indicate the 68% and 95% credible regions, while the diagonal panels show the corresponding one-dimensional marginals. In the anchored analysis, the external Gaussian prior is applied to the effective late-time Hubble scale $H_0^{\text{eff}} = H_0/\sqrt{1 - c_{e0}^2}$ rather than directly to H_0 , which induces the characteristic degeneracy direction in the (H_0, c_{e0}^2) plane.

which is equivalent to analytically marginalizing over a constant offset with a flat prior. Operationally, we profile separately for each cosmological model (HEED and Λ CDM), so each curve is shifted by its own ΔM^* , consistent with standard practice in compressed SN likelihood applications [9, 61]. Consequently, SN data alone do not fix H_0 ; the absolute scale is set only when combined with an absolute ruler such as CC or BAO (through r_d), or by including an explicit external anchor.

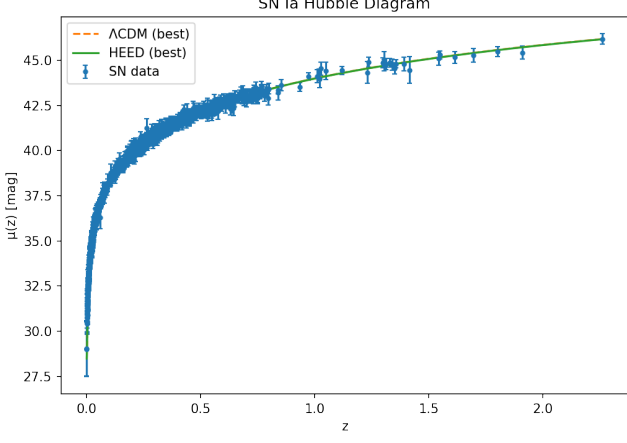


FIG. 4. Pantheon+ SN Ia distance moduli $\mu(z)$ compared to the best-fit HEED (solid) and Λ CDM (dashed) predictions. The fits are shown after profiling over the nuisance offset ΔM (absolute-magnitude/zero-point) as described in the text.

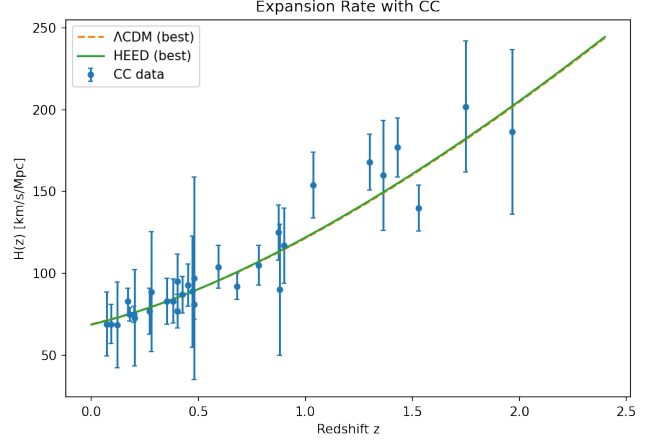


FIG. 5. CC measurements of $H(z)$ with 1σ uncertainties compared to the best-fit HEED (solid) and Λ CDM (dashed) predictions.

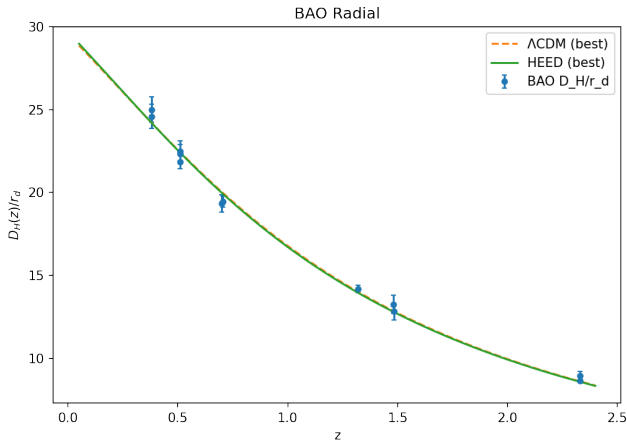


FIG. 6. BAO measurements of the radial (line-of-sight) co-moving distance, $D_H(z)/r_d$ with $D_H \equiv c/H(z)$, compared to the best-fit HEED (solid) and Λ CDM (dashed) predictions.

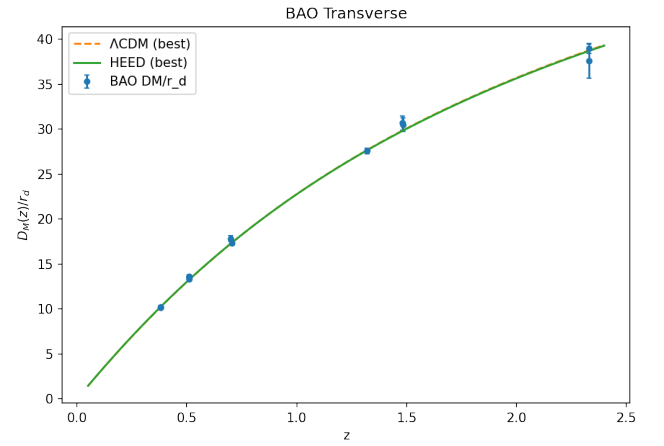


FIG. 7. BAO measurements of the transverse comoving distance, $D_M(z)/r_d$, compared to the best-fit HEED (solid) and Λ CDM (dashed) predictions.

The BAO and CC blocks adopt diagonal Gaussian forms,

$$\chi_{\text{BAO}}^2 = \sum_j \left[\frac{(d_M(z_j)/r_d - (d_M/r_d)_{\text{obs}})^2}{\sigma_{d_M/r_d, j}^2} + \frac{(d_H(z_j)/r_d - (d_H/r_d)_{\text{obs}})^2}{\sigma_{d_H/r_d, j}^2} \right], \quad (34)$$

$$\chi_{\text{CC}}^2 = \sum_{\ell} \frac{(H(z_{\ell}) - H_{\text{obs}})^2}{\sigma_{H, \ell}^2}, \quad (35)$$

which coincide with the usual form $\chi^2 = \mathbf{r}^T \mathbf{C}^{-1} \mathbf{r}$ under the assumptions that reported errors are Gaussian and cross-point covariances are negligible in the compressed products used here.

The corresponding grows log-likelihood is taken as

$$\chi_{\text{RSD}}^2 = \sum_m \frac{[f\sigma_8(z_m; \boldsymbol{\theta}) - (f\sigma_8)_{\text{obs}}]^2}{\sigma_{f\sigma_8, m}^2}, \quad (36)$$

with diagonal errors in this baseline implementation. In practice, the RSD block provides the primary handle on late-time structure growth in our low- z data combination, since the predicted $f\sigma_8(z)$ is obtained by solving the linear

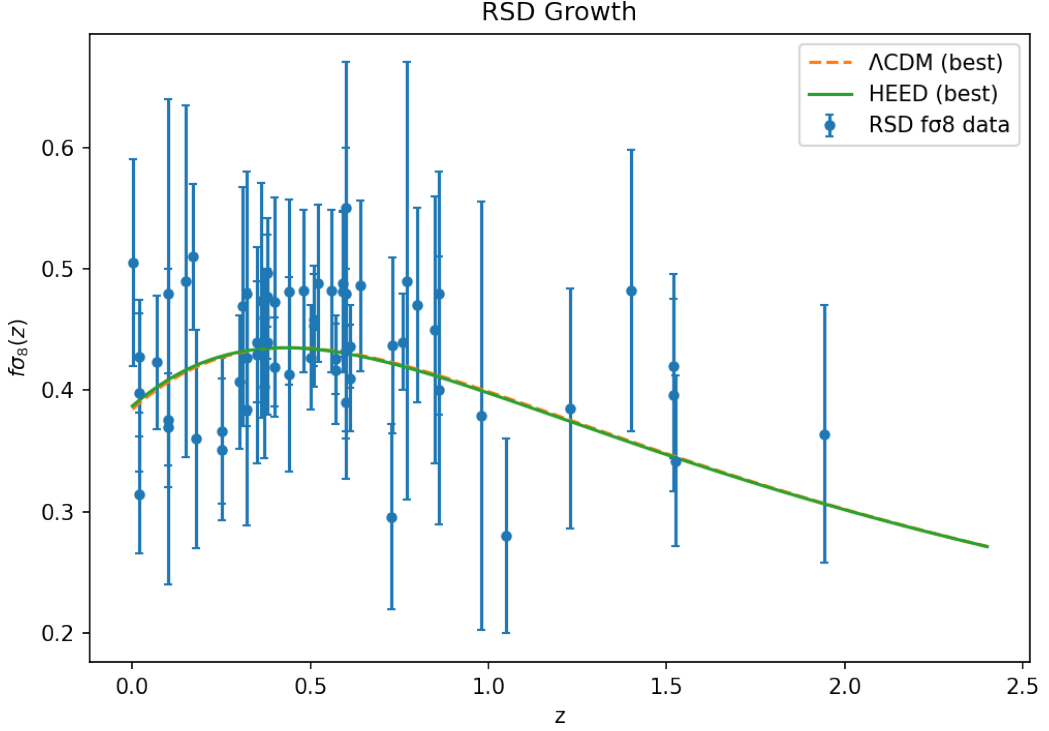


FIG. 8. RSD growth constraints in the HEED framework. Measurements of $f\sigma_8(z)$ with 1σ uncertainties compared to the best-fit predictions for HEED (additive embedding) and Λ CDM. Model curves are obtained by solving the linear growth equation Eq. (21) assuming a smooth (non-clustering) HEED sector, normalizing $D(a=1) = 1$, and computing $f\sigma_8(z) = (d \ln D / d \ln a) \sigma_{8,0} D(a)$ at $a = (1+z)^{-1}$.

growth equation with coefficients determined by the background expansion $H(z)$. Within the assumptions of GR growth and a smooth (non-clustering) HEED sector, this term therefore links the background parameters controlling $H(z)$ to the growth history encoded in $D(a)$ and $f \equiv d \ln D / d \ln a$.

To regularize the growth sector, we include a weak Gaussian prior on σ_8 ,

$$\chi_{\sigma_8}^2 = \left(\frac{\sigma_8 - \sigma_{8,*}}{\sigma_{\sigma_8}} \right)^2, \quad (37)$$

which may be chosen broad enough to avoid importing CMB-dominated information, yet prevents unphysical excursions when the RSD block alone is insufficient to pin down σ_8 in combination with $(\Omega_m, c_{e0}^2, a_t, k)$.

We include three priors/guards, assembled as

$$\chi_{\text{prior}}^2 = \chi_{\text{early}}^2 + \chi_{\text{wall}}^2 + \chi_{H_0^{\text{eff}}}^2. \quad (38)$$

The early-time prior enforces negligible HEED at recombination,

$$\chi_{\text{early}}^2 = \begin{cases} 0, & c_e^2(a_*) \leq \varepsilon, \\ \left(\frac{c_e^2(a_*) - \varepsilon}{\varepsilon} \right)^2 W, & c_e^2(a_*) > \varepsilon, \end{cases} \quad a_* = (1 + 1100)^{-1}, \quad \varepsilon = 10^{-3}, \quad W = 10^4, \quad (39)$$

and the wall prior penalizes approaching $c_e^2 \rightarrow 1$ (where the effective Planck mass $M_*^2 \propto 1 - c_e^2$ would vanish) over the redshift range of the data,

$$\chi_{\text{wall}}^2 = \begin{cases} 0, & \max_{a \in [a_{\text{min}}, 1]} c_e^2(a) \leq c_{\text{wall}}^2, \\ W_{\text{wall}} (\max c_e^2 - c_{\text{wall}}^2)^2, & \text{otherwise,} \end{cases} \quad (40)$$

with $a_{\min} = (1 + z_{\max})^{-1}$ and z_{\max} the largest redshift used in the likelihood.

Finally, in anchored analysis we impose an external Gaussian prior on the *effective* Hubble scale H_0^{eff} , not on H_0 ,

$$\chi_{H_0^{\text{eff}}}^2 = \left(\frac{H_0^{\text{eff}} - H_{0,*}^{\text{eff}}}{\sigma_{H_0^{\text{eff}}}} \right)^2, \quad H_0^{\text{eff}} = \frac{H_0}{\sqrt{1 - c_{e0}^2}}. \quad (41)$$

This prior is not used to infer the Hubble scale from low- z probes alone. Rather, it enables a consistency test: we ask whether HEED can accommodate a locally inferred high late-time expansion rate while remaining compatible with SN, BAO, CC, and RSD constraints that jointly probe distances and growth.

We sample the posterior $\mathcal{P}(\boldsymbol{\theta} \mid \mathbf{d})$ using the affine-invariant ensemble sampler `emcee` [100], and compute marginalized constraints and triangle plots using `GetDist` [101].

B. Posterior constraints and internal consistency of HEED

Figure 3 presents the marginalized one- and two-dimensional posterior distributions for the HEED parameter vector $\{H_0, \Omega_m, c_{e0}^2, a_t, k, \sigma_8\}$, obtained from the joint SN+BAO+CC+RSD likelihood with the priors and profiling procedure specified in Sec. III A. The shaded contours enclose the 68% and 95% credible regions, while the diagonal panels show the corresponding one-dimensional marginals. Complementary to these parameter constraints, the data space fits shown in Figs. 4, 5, 6, 7, 8 demonstrate that the best fit HEED and Λ CDM predictions are nearly indistinguishable across the low redshift observables considered here (Pantheon+ $\mu(z)$, CC $H(z)$, BAO D_M/r_d and D_H/r_d , and RSD $f\sigma_8$), with no systematic preference visible at the level of current uncertainties. We therefore interpret the posterior in Fig. 3 primarily as a consistency statement: within the adopted additive HEED embedding and priors, a late time entanglement driven modification of the expansion history can be introduced without spoiling established low- z distance and growth constraints.

A number of qualitative and quantitative features demonstrate that the inferred constraints are internally consistent with the physical assumptions underlying HEED.

Hubble constant. As pointed in Sec. III A, in the present analysis, the posterior is conditioned on an external Gaussian prior (“anchor”) on the effective late-time Hubble scale centered at $H_{0,*}^{\text{eff}} = 73 \text{ km s}^{-1} \text{ Mpc}^{-1}$ as inferred from [2]. Accordingly, the chains do not *infer* an upward shift of the Hubble scale relative to CMB-only analyses; rather, they test whether the HEED background and growth sector can remain compatible with SN+BAO+CC+RSD while accommodating a high locally inferred expansion rate. Because in the additive HEED embedding Eq. (27), the anchor does not force the sampled parameter H_0 itself to be large. Rather, the posterior realizes $H_0^{\text{eff}} \simeq 73 \text{ km s}^{-1} \text{ Mpc}^{-1}$ with moderate values of H_0 provided $c_{e0}^2 > 0$, leading to a pronounced anti-correlation between H_0 and c_{e0}^2 in the marginalized posterior shown in Fig. 3.

Matter density. The matter density parameter Ω_m is constrained at the level typical of low-redshift analyses, with a clear anti-correlation with H_0 . This degeneracy is expected: an increase in the late-time expansion rate induced by HEED must be compensated by a corresponding adjustment in Ω_m in order to preserve the BAO distance measurements. The inferred values of the matter density parameter remain within the range allowed by late time large scale structure (LSS) probes, including BAO geometry, RSD measurements and galaxy clustering with weak lensing combinations. In particular, the moderate increase in Ω_m relative to Λ CDM is compensated by the HEED-induced suppression of late-time growth, so that the predicted $f\sigma_8(z)$ remains consistent with current observational constraints.

Present-day HEED amplitude. A central result of the analysis is that the posterior for the HEED amplitude c_{e0}^2 peaks decisively away from zero. Pure Λ CDM, corresponding to $c_{e0}^2 = 0$, lies in the tail of the posterior. At the same time, the data strongly disfavor values approaching the physical wall $c_e^2 \rightarrow 1$, ensuring a positive effective Planck mass $M_*^2 \propto 1 - c_e^2$ and the absence of instabilities. This provides direct phenomenological support for a nonvanishing late-time horizon entanglement deficit.

Activation epoch. The activation scale factor a_t is constrained to lie in the range $a_t \sim 0.4 - 0.6$, corresponding to a redshift $z_t \sim 0.7 - 1.5$. This places the onset of HEED squarely in the late universe, well after recombination and the baryon-drag epoch. As a result, early universe observables such as the sound horizon remain unaffected, while the late-time expansion history is modified in precisely the redshift range probed by SN, BAO, and CC data.

Activation sharpness. The shape parameter k , which controls the sharpness of the HEED switch-on, is only weakly constrained by current data and exhibits broad, possibly multi-modal posteriors. This behavior is expected: existing low-redshift probes are primarily sensitive to the integrated effect of the late-time expansion rate rather than to the detailed functional form of the transition. Consequently, k effectively plays the role of a nuisance parameter at present precision.

Growth amplitude. The posterior for σ_8 is mildly shifted toward lower values compared to the Planck Λ CDM determination [1]. This reflects the fact that the enhanced late-time expansion induced by HEED leads to a modest suppression of structure growth at $z \lesssim 1$. The resulting values of σ_8 and the correlated predictions for $f\sigma_8(z)$ remain compatible with RSD measurements, while potentially easing the weak-lensing clustering-amplitude (S_8) tension, i.e. the preference of several stage-III cosmic-shear analyses for $S_8 \equiv \sigma_8 \sqrt{\Omega_m}/0.3$ values lower than the CMB-inferred Planck Λ CDM prediction (e.g. KiDS-1000 and DES Y3) [102–104].

Correlation structure. The two-dimensional marginalized posteriors exhibit a pattern of correlations that can be understood directly from the structure of the HEED background and from the combination of low-redshift probes employed. Because the analysis is conditioned on an external prior on the effective late-time Hubble scale H_0^{eff} , the sampled parameters H_0 and c_{e0}^2 are strongly anti-correlated. This follows from the additive HEED relation Eq. (27): for a fixed H_0^{eff} , a larger entanglement deficit requires a smaller underlying H_0 . The corresponding elongated contours in the (H_0, c_{e0}^2) plane therefore reflect a purely kinematic degeneracy rather than a physical instability.

A positive correlation is observed between c_{e0}^2 and Ω_m . In the anchored analysis, increasing c_{e0}^2 lowers the sampled value of H_0 , which tends to increase comoving distances at fixed dimensionless expansion rate. To preserve the BAO and CC constraints on distances and $H(z)$, the fit compensates by increasing Ω_m , which raises $Q(z)$ at intermediate redshifts and reduces the integrated distances. This correlation therefore encodes the geometric balance required to maintain consistency with BAO measurements in the presence of a late-time entanglement contribution.

The correlation between c_{e0}^2 and σ_8 reflects the expansion-growth interplay probed by RSDs. A larger entanglement deficit enhances the late-time expansion rate, which mildly suppresses the growth of linear perturbations at $z \lesssim 1$. This suppression can be partially offset by a correlated adjustment of the present-day fluctuation amplitude σ_8 , ensuring that the predicted $f\sigma_8(z)$ remains compatible with RSD data. As a result, the joint posterior occupies a region in parameter space where background expansion and structure growth are simultaneously consistent.

Finally, the activation parameters (a_t, k) exhibit broad degeneracies with c_{e0}^2 and with each other. Current low-redshift data primarily constrain the integrated effect of the HEED contribution on the expansion history rather than the detailed time profile of its onset. Consequently, the sharpness parameter k is only weakly constrained, while the activation epoch a_t is restricted to late times by the requirement of early universe safety.

Implications. Taken together, the posterior distributions demonstrate that HEED operates in the regime it was designed for: it activates only at late times, modifies the expansion history at the few percent level, preserves early universe physics, and remains consistent with structure-growth constraints. While the current data do not yet yield a statistically decisive preference over Λ CDM, the results show that HEED can significantly alleviate the Hubble tension without introducing pathologies or fine-tuning, and they motivate further tests with upcoming LSS and CMB-LSS cross-correlation data. These results should therefore be interpreted as an *anchored consistency test* (high H_0^{eff} imposed), rather than as a free low- z determination of the Hubble scale.

For the parameter values favored by Fig. 3, the best-fit HEED and Λ CDM curves in Figs. 4, 5, 6, 7, 8 are nearly indistinguishable within the current observational uncertainties. This behavior is expected. First, the low-redshift data blocks employed here—SN Ia distance moduli, compressed BAO distances, CC $H(z)$ points, and RSD $f\sigma_8(z)$ measurements—primarily constrain integrated distance and expansion combinations, and therefore admit substantial degeneracies among late time expansion histories. In this regime, distinct parameterizations can map onto very similar $H(z)$ and distance predictions once their parameters are adjusted to satisfy the same geometric constraints. Second, our SN likelihood profiles over the nuisance offset ΔM , so SN data constrain relative distances and provide only weak leverage on the absolute expansion scale. Finally, in anchored analyses the external Gaussian prior is applied to the effective late time Hubble scale H_0^{eff} rather than directly to H_0 . Consequently, the parameters H_0 and c_{e0}^2 can trade off along the degeneracy direction implied by the additive HEED embedding while keeping H_0^{eff} (and hence much of the low- z expansion history) close to the anchored value. The close overlap of the corresponding best fit curves thus indicates that HEED can accommodate a nonzero late time entanglement amplitude without spoiling established low- z distance and growth constraints, while also highlighting that present data have limited power to distinguish HEED from Λ CDM at the level of background and linear growth observables.

IV. CONCLUSIONS

We have developed and confronted a simple realization of HEED as a late time, IR contribution to the cosmic energy budget. In HEED, the apparent (Hubble) horizon acts as an entanglement screen whose quantum correlations do not fully saturate the Bekenstein–Hawking entropy at late times. The resulting deficit is mapped, via horizon thermodynamics and equipartition, into a smooth bulk component whose characteristic scaling is $\rho_{\text{HEED}} \propto H^2/G$. This scaling is of precisely the magnitude required to affect late time expansion while remaining negligible at recombination, and it is qualitatively distinct from free-field vacuum effects that generate parametrically smaller $\delta\rho \sim H^4$ corrections.

At the level of internal consistency, HEED is compatible with standard requirements of cosmological model building. In the additive embedding used throughout this work, the entanglement sector modifies the background through an algebraic rescaling of the Friedmann equation while preserving the Bianchi identity and covariant conservation of matter, $\dot{\rho}_m + 3H\rho_m = 0$. By construction the model remains physical provided $0 \leq c_e^2(a) < 1$, which ensures a positive effective Planck mass $M_*^2 \propto 1 - c_e^2$ and avoids the pathologies associated with vanishing gravitational coupling. Interpreted as an effective, nonpropagating IR sector, HEED can transiently realize an effective equation of state below -1 during its switch on without implying ghost instabilities, since no additional propagating degree of freedom is introduced.

Phenomenologically, HEED is predictive and testable. The characteristic late-time activation yields a few percent upward shift of the effective Hubble scale, modifies distances at $z \lesssim \mathcal{O}(1)$, and produces a mild suppression of linear growth together with a modest enhancement of the late integrated Sachs–Wolfe (ISW) effect. Importantly, the best-fit HEED and Λ CDM curves across the low redshift observables considered (SN Ia, BAO, CC, and RSD) are nearly indistinguishable within current uncertainties, indicating that the HEED mechanism can be switched on at late times without spoiling established distance and growth constraints. This near-degeneracy also emphasizes that robust discrimination will require either higher precision low- z measurements, additional growth probes (e.g. weak lensing and CMB lensing), or joint analyses with CMB–LSS cross correlations that directly test the ISW response.

Finally, we stress the conceptual advantage of anchoring the IR contribution to a quasi-local horizon. Teleological issues refer to pathologies that arise when present time quantities depend on the *entire future history* of the universe. The future event horizon is a global object: its existence and radius at time t depend on whether signals emitted after t will ever reach the observer, which requires knowledge of the spacetime to arbitrarily late times. Consequently, models that set an IR cutoff by the future event horizon make the present energy density a functional of the future expansion history, leading to acausality and nonlocal in-time evolution. In contrast, the apparent (Hubble) horizon in FLRW is determined quasi-locally on each time slice and underlies local horizon thermodynamics and derivations of the Friedmann equations via first-law equipartition arguments. HEED ties its IR contribution to the apparent (Hubble) horizon and therefore remains local in time, avoiding the teleology inherent to future event horizon models [18, 22, 25, 60].

Several extensions are immediate. A next step is a full model comparison with Λ CDM using consistent covariances for SN and BAO products and including additional growth information (cosmic shear, CMB lensing, cluster abundance). On the theory side, the HEED parameterization can be sharpened by constructing microphysical models for the deficit function $\delta(a)$ (or $c_e^2(a)$), e.g. in terms of horizon mutual information, entanglement–wedge capacity, or Gauss law constraints on gravitational dressing. These developments would move HEED from a phenomenological IR mechanism toward a predictive, first principles account of how horizon entanglement can influence late time cosmology.

ACKNOWLEDGEMENTS

The work of R.K. and J.S. was partially supported by the Kakos Endowed Chair in Science Fellowship.

Appendix A: Entanglement First Law, Modular Energy, and the H^4 Scaling

Consider a quantum field theory (beginning with a free/conformal scalar) in 3+1 dimensions on a spatial slice of a FLRW spacetime that is close to de Sitter with Hubble parameter H . Let B be a ball of radius R (possibly of order the Hubble radius) on a constant-time slice. For a conformal field theory (CFT) in flat space, the vacuum modular Hamiltonian \mathcal{H}_B for a ball is local and can be written as

$$\mathcal{H}_B = 2\pi \int_B d^3x \frac{R^2 - r^2}{2R} T_{00}(x) + \text{const.}, \quad (\text{A1})$$

as obtained from the conformal map between the ball and a hyperbolic/Rindler wedge [54, 55].

The first law of entanglement states that for small state/geometry variations

$$\delta S_B = \delta \langle \mathcal{H}_B \rangle = 2\pi \int_B d^3x \frac{R^2 - r^2}{2R} \delta \langle T_{00}(x) \rangle, \quad (\text{A2})$$

which is the linearized relation between entanglement entropy and modular energy (relative entropy at first order) [56, 57].

In a smooth curved background, the renormalized vacuum stress tensor of a four-dimensional CFT is controlled by the conformal (trace) anomaly, therefore in de Sitter (Weyl-flat with $C_{\mu\nu\rho\sigma} = 0$) one has

$$\langle T_{\mu\nu} \rangle_{\text{vac}} = c_A H^4 g_{\mu\nu}, \quad (\text{A3})$$

with c_A fixed by the type-A anomaly and field content [58]. Dimensional analysis in 4D implies $\langle T_{\mu\nu} \rangle \propto H^4$ in the IR. For a small deformation from Minkowski/adiabatic vacuum to (quasi) de Sitter,

$$\delta\langle T_{00} \rangle \sim \sigma H^4, \quad (\text{A4})$$

where σ is a dimensionless coefficient set by field content.

Using the spherical weight and

$$\int_0^R 4\pi r^2 (R^2 - r^2) dr = \frac{8\pi}{15} R^5,$$

Eq. (A2) gives

$$\begin{aligned} \delta S_B &= 2\pi \frac{1}{2R} \delta\langle T_{00} \rangle \int_B d^3x (R^2 - r^2) \\ &= \frac{8\pi^2}{15} R^4 \delta\langle T_{00} \rangle \sim \frac{8\pi^2}{15} R^4 \sigma H^4. \end{aligned} \quad (\text{A5})$$

For a ball in a CFT vacuum, the modular (entanglement) temperature is $T_{\text{mod}} = 1/(2\pi R)$. A Clausius-like relation then yields

$$\begin{aligned} \delta E_B &= T_{\text{mod}} \delta S_B = \frac{1}{2\pi R} \cdot \frac{8\pi^2}{15} R^4 \delta\langle T_{00} \rangle \\ &= \frac{4\pi}{15} R^3 \delta\langle T_{00} \rangle, \end{aligned} \quad (\text{A6})$$

and dividing by the ball volume $V_B = (4\pi/3)R^3$ gives the renormalized energy-density shift

$$\delta\rho = \frac{\delta E_B}{V_B} = \frac{1}{5} \delta\langle T_{00} \rangle \sim \mathcal{O}(H^4). \quad (\text{A7})$$

Thus, free/CFT vacuum contributions to the late-time energy density scale as H^4 and are negligible compared to the critical density $\rho_{\text{crit}} = 3H^2/(8\pi G)$:

$$\frac{\delta\rho}{\rho_{\text{crit}}} \sim \left(\frac{H}{M_{\text{Pl}}} \right)^2 \ll 1. \quad (\text{A8})$$

A careful modular Hamiltonian first law analysis shows that standard free-field entanglement yields only $\mathcal{O}(H^4)$ energy density corrections at late times. Hence, any phenomenologically relevant $\sim H^2/G$ component must arise from IR/holographic or nonlocal/emergent physics tied to the horizon scale, not from the UV area law of free fields.

The H^4 scaling derived above concerns the finite, renormalized, state-dependent IR response of free/CFT fields to a smooth (quasi-)de Sitter background, for which the only available macroscopic scale is H and thus $\delta\langle T_{\mu\nu} \rangle \propto H^4 g_{\mu\nu}$. By contrast, the UV part of vacuum entanglement across a smooth surface produces a nonuniversal area-law divergence, $S_{\text{ent}} \sim \eta A/\epsilon^2$, where ϵ is a short-distance regulator (UV cutoff) and η depends on field content and the scheme. In semiclassical gravity, the same UV modes renormalize the Einstein–Hilbert coupling (and higher-curvature terms), so that the geometric entropy is expressed in terms of the renormalized Newton constant G_{ren} and the UV area term is not an additional dynamical component [32, 59, 105]. Counting the area law again as an energy density would therefore double count degrees of freedom already absorbed into G_{ren} . Consequently, free-field entanglement does not generate a late-time $\mathcal{O}(H^2/G)$ contribution: light fields continue to give $\mathcal{O}(H^4)$ IR effects, while heavy fields mainly renormalize local couplings.

Appendix B: Data

TABLE I. CC $H(z)$ measurements (classic 31-point, typically treated as non-correlated). Uncertainties are 1σ .

z	$H(z)$ [km s $^{-1}$ Mpc $^{-1}$]	σ [km s $^{-1}$ Mpc $^{-1}$]	Refs	Year
0.07	69.0	19.6	[62]	2014
0.09	69.0	12.0	[63]	2005
0.12	68.6	26.2	[62]	2014
0.17	83.0	8.0	[63]	2005
0.179	75.0	4.0	[64]	2012
0.199	75.0	5.0	[64]	2012
0.200	72.9	29.6	[62]	2014
0.270	77.0	14.0	[63]	2005
0.280	88.8	36.6	[62]	2014
0.352	83.0	14.0	[64]	2012
0.3802	83.0	13.5	[65]	2016
0.400	95.0	17.0	[63]	2005
0.4004	77.0	10.2	[65]	2016
0.4247	87.1	11.2	[65]	2016
0.4497	92.8	12.9	[65]	2016
0.470	89.0	34.0	[67]	2017
0.4783	80.9	9.0	[65]	2016
0.480	97.0	62.0	[68]	2010
0.593	104.0	13.0	[64]	2012
0.680	92.0	8.0	[64]	2012
0.781	105.0	12.0	[64]	2012
0.875	125.0	17.0	[64]	2012
0.880	90.0	40.0	[68]	2010
0.900	117.0	23.0	[63]	2005
1.037	154.0	20.0	[64]	2012
1.300	168.0	17.0	[63]	2005
1.363	160.0	33.6	[66]	2015
1.430	177.0	18.0	[63]	2005
1.530	140.0	14.0	[63]	2005
1.750	202.0	40.0	[63]	2005
1.965	186.5	50.4	[66]	2015

TABLE II. BAO transverse comoving and radial (Hubble) distance measurements, shown jointly as $D_M(z)/r_d$ and $D_H(z)/r_d$ with 1σ uncertainties. Numerical values are taken from Table 4 of Ref. [10], Table III of Ref. [11] and Table IV of Ref. [4]. BOSS/eBOSS BAO data are also summarized in Ref. [106].

z	D_M/r_d	σ_{D_M/r_d}	D_H/r_d	σ_{D_H/r_d}	Refs	Year
0.38	10.23	0.17	25.00	0.76	[11]	2020
0.38	10.16	0.18	24.59	0.72	[10]	2016
0.51	13.588	0.167	21.863	0.425	[4]	2025
0.51	13.36	0.21	22.33	0.58	[11]	2020
0.51	13.6	0.2	22.49	0.62	[10]	2016
0.70	17.86	0.33	19.33	0.53	[11]	2020
0.706	17.351	0.177	19.455	0.33	[4]	2025
1.321	27.601	0.318	14.176	0.221	[4]	2025
1.48	30.69	0.80	13.26	0.55	[11]	2020
1.484	30.512	0.76	12.817	0.516	[4]	2025
2.33	38.988	0.531	8.632	0.101	[4]	2025
2.33	37.6	1.9	8.93	0.28	[11]	2020

^{*} alexandre.sakharov@cern.ch[†] rostislav.konoplich@manhattan.edu[‡] gogber@gmail.com[§] jsimoni02@manhattan.edu

TABLE III. RSD growth rate measurements $f\sigma_8(z)$ and 1σ uncertainties. Data acquired from Table II of Ref. [91].

Index	Dataset	z	$f\sigma_8(z)$	Refs	Year
1	SDSS-LRG	0.35	0.440 ± 0.050	[92]	2006
2	VVDS	0.77	0.490 ± 0.180	[92]	2009
3	2dFGRS	0.17	0.510 ± 0.060	[92]	2009
4	2MRS	0.02	0.314 ± 0.048	[83], [84]	2010
5	SnIa+IRAS	0.02	0.398 ± 0.065	[84], [107]	2011
6	SDSS-LRG-200	0.25	0.3512 ± 0.0583	[93]	2011
7	SDSS-LRG-200	0.37	0.4602 ± 0.0378	[93]	2011
8	SDSS-LRG-60	0.25	0.3665 ± 0.0601	[93]	2011
9	SDSS-LRG-60	0.37	0.4031 ± 0.0586	[93]	2011
10	WiggleZ	0.44	0.413 ± 0.080	[75]	2012
11	WiggleZ	0.60	0.390 ± 0.063	[75]	2012
12	WiggleZ	0.73	0.437 ± 0.072	[75]	2012
13	6dFGS	0.067	0.423 ± 0.055	[85]	2012
14	SDSS-BOSS	0.30	0.407 ± 0.055	[74]	2012
15	SDSS-BOSS	0.40	0.419 ± 0.041	[74]	2012
16	SDSS-BOSS	0.50	0.427 ± 0.043	[74]	2012
17	SDSS-BOSS	0.60	0.433 ± 0.067	[74]	2012
18	Vipers	0.80	0.470 ± 0.080	[76]	2013
19	SDSS-DR7-LRG	0.35	0.429 ± 0.089	[94]	2013
20	GAMA	0.18	0.360 ± 0.090	[98]	2013
21	GAMA	0.38	0.440 ± 0.060	[98]	2013
22	BOSS-LOWZ	0.32	0.384 ± 0.095	[69]	2013
23	SDSS DR10 and DR11	0.32	0.480 ± 0.100	[69]	2013
24	SDSS DR10 and DR11	0.57	0.417 ± 0.045	[69]	2013
25	SDSS-MGS	0.15	0.490 ± 0.145	[95]	2015
26	SDSS-veloc	0.10	0.370 ± 0.130	[96]	2015
27	FastSound	1.40	0.482 ± 0.116	[87]	2015
28	SDSS-CMASS	0.59	0.488 ± 0.060	[71]	2016
29	BOSS DR12	0.38	0.497 ± 0.045	[10]	2016
30	BOSS DR12	0.51	0.458 ± 0.038	[10]	2016
31	BOSS DR12	0.61	0.436 ± 0.034	[10]	2016
32	BOSS DR12	0.38	0.477 ± 0.051	[72]	2016
33	BOSS DR12	0.51	0.453 ± 0.050	[72]	2016
34	BOSS DR12	0.61	0.410 ± 0.044	[72]	2016
35	Vipers v7	0.76	0.440 ± 0.040	[77]	2016
36	Vipers v7	1.05	0.280 ± 0.080	[77]	2016
37	BOSS LOWZ	0.32	0.427 ± 0.056	[70]	2016
38	BOSS CMASS	0.57	0.426 ± 0.029	[70]	2016
39	Vipers	0.727	0.296 ± 0.0765	[78]	2016
40	6dFGS+SnIa	0.02	0.428 ± 0.0465	[86]	2016
41	Vipers	0.60	0.480 ± 0.120	[79]	2016
42	Vipers	0.86	0.480 ± 0.100	[79]	2016
43	Vipers PDR-2	0.60	0.550 ± 0.120	[80]	2016
44	Vipers PDR-2	0.86	0.400 ± 0.110	[80]	2016
45	SDSS DR13	0.10	0.480 ± 0.160	[97]	2016
46	2MTF	0.001	0.505 ± 0.085	[82]	2017
47	Vipers PDR-2	0.85	0.450 ± 0.110	[81]	2017
48	BOSS DR12	0.31	0.469 ± 0.098	[73]	2017
49	BOSS DR12	0.36	0.474 ± 0.097	[73]	2017
50	BOSS DR12	0.40	0.473 ± 0.086	[73]	2017
51	BOSS DR12	0.44	0.481 ± 0.076	[73]	2017
52	BOSS DR12	0.48	0.482 ± 0.067	[73]	2017
53	BOSS DR12	0.52	0.488 ± 0.065	[73]	2017
54	BOSS DR12	0.56	0.482 ± 0.067	[73]	2017
55	BOSS DR12	0.59	0.481 ± 0.066	[73]	2017
56	BOSS DR12	0.64	0.486 ± 0.070	[73]	2017
57	SDSS DR7	0.10	0.376 ± 0.038	[99]	2017
58	SDSS-IV	1.52	0.420 ± 0.076	[89]	2018
59	SDSS-IV	1.52	0.396 ± 0.079	[90]	2018
60	SDSS-IV	0.978	0.379 ± 0.176	[88]	2018
61	SDSS-IV	1.23	0.385 ± 0.099	[88]	2018
62	SDSS-IV	1.526	0.342 ± 0.070	[88]	2018
63	SDSS-IV	1.944	0.364 ± 0.106	[88]	2018

[1] Planck Collaboration, N. Aghanim, *et al.*, Planck 2018 results. vi. cosmological parameters, *Astronomy & Astrophysics* **641**, A6 (2020), arXiv:1807.06209 [astro-ph.CO].

[2] A. G. Riess *et al.*, A comprehensive measurement of the local value of the hubble constant with $1 \text{ km s}^{-1} \text{ mpc}^{-1}$ uncertainty from the hubble space telescope and the sh0es team, *The Astrophysical Journal Letters* **934**, L7 (2022), arXiv:2112.04510 [astro-ph.CO].

[3] A. G. Adame *et al.* (DESI), DESI 2024 VI: cosmological constraints from the measurements of baryon acoustic oscillations, *JCAP* **02**, 021, arXiv:2404.03002 [astro-ph.CO].

[4] M. Abdul Karim *et al.* (DESI), DESI DR2 results. II. Measurements of baryon acoustic oscillations and cosmological constraints, *Phys. Rev. D* **112**, 083515 (2025), arXiv:2503.14738 [astro-ph.CO].

[5] E. Di Valentino, O. Mena, S. Pan, L. Visinelli, W. Yang, A. Melchiorri, D. F. Mota, A. G. Riess, and J. Silk, In the realm of the hubble tension: A review of solutions, *Classical and Quantum Gravity* **38**, 153001 (2021), arXiv:2103.01183 [astro-ph.CO].

[6] E. Abdalla, G. F. Abellán, A. Aboubrahim, *et al.*, Cosmology intertwined: A review of the particle physics, astrophysics, and cosmology associated with the cosmological tensions and anomalies, *Journal of High Energy Astrophysics* **34**, 49 (2022), arXiv:2203.06142 [astro-ph.CO].

[7] N. Schöneberg, G. Franco Abellán, A. Pérez Sánchez, S. J. Witte, V. Poulin, and J. Lesgourgues, The H0 Olympics: A fair ranking of proposed models, *Phys. Rept.* **984**, 1 (2022), arXiv:2107.10291 [astro-ph.CO].

[8] E. Di Valentino *et al.* (CosmoVerse Network), The CosmoVerse White Paper: Addressing observational tensions in cosmology with systematics and fundamental physics, *Phys. Dark Univ.* **49**, 101965 (2025), arXiv:2504.01669 [astro-ph.CO].

[9] D. Scolnic, D. Brout, A. Carr, A. G. Riess, T. M. Davis, A. Dwomoh, D. O. Jones, N. Ali, W. D. Kenworthy, E. R. Peterson, K. Said, B. Popovic, G. Taylor, and et al., The pantheon+ analysis: The full data set and light-curve release, *Astrophysical Journal* **938**, 113 (2022), arXiv:2112.03863 [astro-ph.CO].

[10] S. Alam *et al.* (BOSS), The clustering of galaxies in the completed SDSS-III Baryon Oscillation Spectroscopic Survey: cosmological analysis of the DR12 galaxy sample, *Mon. Not. Roy. Astron. Soc.* **470**, 2617 (2017), arXiv:1607.03155 [astro-ph.CO].

[11] S. Alam, M. Ishak, S. Ho, W. J. Percival, A. J. Ross, G.-B. Zhao, and et al., Completed sdss-iv extended baryon oscillation spectroscopic survey: Cosmological implications from two decades of spectroscopic surveys at the apache point observatory, *Physical Review D* **103**, 083533 (2021), arXiv:2007.08991 [astro-ph.CO].

[12] M. M. Ivanov, E. McDonough, J. C. Hill, M. Simonović, M. W. Toomey, S. Alexander, and M. Zaldarriaga, Constraining early dark energy with large-scale structure, *Physical Review D* **102**, 103502 (2020), arXiv:2006.11235 [astro-ph.CO].

[13] J. C. Hill, E. Calabrese, S. Aiola, *et al.*, Atacama cosmology telescope: Constraints on prerecombination early dark energy, *Physical Review D* **105**, 123536 (2022), arXiv:2109.04451 [astro-ph.CO].

[14] A. G. Cohen, D. B. Kaplan, and A. E. Nelson, Effective field theory, black holes, and the cosmological constant, *Physical Review Letters* **82**, 4971 (1999).

[15] M. Li, A model of holographic dark energy, *Physics Letters B* **603**, 1 (2004), arXiv:hep-th/0403127 [hep-th].

[16] S. D. H. Hsu, Entropy bounds and dark energy, *Physics Letters B* **594**, 13 (2004), arXiv:hep-th/0403052 [hep-th].

[17] S. Wang, Y. Wang, and M. Li, Holographic dark energy, *Physics Reports* **696**, 1 (2017), arXiv:1612.00345 [astro-ph.CO].

[18] G. W. Gibbons and S. W. Hawking, Cosmological event horizons, thermodynamics, and particle creation, *Physical Review D* **15**, 2738 (1977).

[19] J. D. Bekenstein, Black holes and entropy, *Phys. Rev. D* **7**, 2333 (1973).

[20] S. W. Hawking, Particle creation by black holes, *Commun. Math. Phys.* **43**, 199 (1975).

[21] R. M. Wald, Black hole entropy is the Noether charge, *Phys. Rev. D* **48**, R3427 (1993).

[22] T. Padmanabhan, Thermodynamical Aspects of Gravity: New insights, *Rep. Prog. Phys.* **73**, 046901 (2010), arXiv:0911.5004 [gr-qc].

[23] T. Padmanabhan, Equipartition of energy in the horizon degrees of freedom and the emergence of gravity, *Mod. Phys. Lett. A* **25**, 1129 (2010), arXiv:0912.3165 [gr-qc].

[24] E. P. Verlinde, On the origin of gravity and the laws of Newton, *JHEP* **04**, 029, arXiv:1001.0785 [hep-th].

[25] T. Padmanabhan, Emergence and Expansion of Cosmic Space as due to the Quest for Holographic Equipartition, 1206.4916 (2012), arXiv preprint, arXiv:1206.4916 [hep-th].

[26] H. Casini and M. Huerta, Entanglement entropy in free quantum field theory, *Journal of Physics A: Mathematical and Theoretical* **42**, 504007 (2009), arXiv:0905.2562 [hep-th].

[27] W. Donnelly and L. Freidel, Local subsystems in gauge theory and gravity, *Journal of High Energy Physics* **2016**, 102 (2016), arXiv:1601.04744 [hep-th].

[28] D. Harlow, Jerusalem lectures on black holes and quantum information, *Reviews of Modern Physics* **88**, 015002 (2017), arXiv:1409.1231 [hep-th].

[29] L. Bombelli, R. K. Koul, J. Lee, and R. D. Sorkin, Quantum source of entropy for black holes, *Physical Review D* **34**, 373 (1986).

[30] M. Srednicki, Entropy and area, *Physical Review Letters* **71**, 666 (1993), arXiv:hep-th/9303048 [hep-th].

[31] L. Susskind and J. Uglum, Black hole entropy in canonical quantum gravity and superstring theory, *Phys. Rev. D* **50**, 2700 (1994), arXiv:hep-th/9401070.

[32] S. N. Solodukhin, Entanglement entropy of black holes, *Living Rev. Rel.* **14**, 8 (2011), arXiv:1104.3712 [hep-th].

[33] J. H. Cooperman and M. A. Luty, Renormalization of entanglement entropy and the gravitational effective action, *Journal of High Energy Physics* **2014**, 045 (2014), arXiv:1302.1878 [hep-th].

[34] N. Engelhardt and A. C. Wall, Quantum extremal surfaces: Holographic entanglement entropy beyond the classical regime, *Journal of High Energy Physics* **2015**, 073 (2015), arXiv:1408.3203 [hep-th].

[35] T. Jacobson, Entanglement equilibrium and the Einstein equation, *Phys. Rev. Lett.* **116**, 201101 (2016), arXiv:1505.04753 [gr-qc].

[36] N. Lashkari, M. B. McDermott, and M. V. Raamsdonk, Gravitational dynamics from entanglement “thermodynamics”, *JHEP* **04**, 195, arXiv:1308.3716 [hep-th].

[37] R. Bousso, The holographic principle, *Reviews of Modern Physics* **74**, 825 (2002), arXiv:hep-th/0203101 [hep-th].

[38] K. S. Thorne, R. H. Price, and D. A. Macdonald, *Black Holes: The Membrane Paradigm* (Yale University Press, 1986).

[39] E. Bellini and M. Sawicki, Maximal freedom at minimum cost: linear large-scale structure in general modifications of gravity, *Journal of Cosmology and Astroparticle Physics* **2014** (07), 050, arXiv:1404.3713 [astro-ph.CO].

[40] R. Kase and S. Tsujikawa, Dark energy in horndeski theories after gw170817: A review, *International Journal of Modern Physics D* **28**, 1942005 (2019), arXiv:1809.08735 [gr-qc].

[41] R. M. Wald, *General Relativity* (University of Chicago Press, 1984).

[42] S. M. Carroll, *Spacetime and Geometry: An Introduction to General Relativity* (Addison-Wesley, 2004).

[43] R. R. Caldwell, A phantom menace? cosmological consequences of a dark energy component with super-negative equation of state, *Physics Letters B* **545**, 23 (2002), arXiv:astro-ph/9908168 [astro-ph].

[44] A. Vikman, Can dark energy evolve to the phantom?, *Physical Review D* **71**, 023515 (2005), arXiv:astro-ph/0407107 [astro-ph].

[45] G. Gubitosi, F. Piazza, and F. Vernizzi, The effective field theory of dark energy, *Journal of Cosmology and Astroparticle Physics* **2013** (02), 032, arXiv:1210.0201 [hep-th].

[46] J. K. Bloomfield, E. E. Flanagan, M. Park, and S. Watson, Dark energy or modified gravity? an effective field theory approach, *Physical Review D* **88**, 083510 (2013), arXiv:1211.7054 [astro-ph.CO].

[47] T. Kobayashi, M. Yamaguchi, and J. Yokoyama, Generalized g-inflation: Inflation with the most general second-order field equations, *Progress of Theoretical Physics* **126**, 511 (2011), arXiv:1105.5723 [hep-th].

[48] C. Deffayet, O. Pujolàs, I. Sawicki, and A. Vikman, Imperfect dark energy from kinetic gravity braiding, *JCAP* **10**, 026, arXiv:1008.0048 [hep-th].

[49] P. J. E. Peebles, The large-scale structure of the universe, Princeton University Press (1980).

[50] S. Dodelson, *Modern Cosmology* (Academic Press, 2003).

[51] E. V. Linder, Cosmic growth history and expansion history, *Physical Review D* **72**, 043529 (2005), arXiv:astro-ph/0507263 [astro-ph].

[52] N. Kaiser, Clustering in real space and in redshift space, *Monthly Notices of the Royal Astronomical Society* **227**, 1 (1987).

[53] A. J. S. Hamilton, Linear redshift distortions: a review, In: *The Evolving Universe* (Kluwer) , 185 (1998), arXiv:astro-ph/9708102 [astro-ph].

[54] H. Casini, M. Huerta, and R. C. Myers, Towards a derivation of holographic entanglement entropy, *JHEP* **05**, 036, arXiv:1102.0440 [hep-th].

[55] M. J. S. Beach, J. Lee, C. Rabideau, and M. Van Raamsdonk, Entanglement entropy from one-point functions in holographic states, *JHEP* **06**, 085, arXiv:1604.05308 [hep-th].

[56] J. Bhattacharya, M. Nozaki, T. Takayanagi, and T. Ugajin, Thermodynamical Property of Entanglement Entropy for Excited States, *Phys. Rev. Lett.* **110**, 091602 (2013), arXiv:1212.1164 [hep-th].

[57] D. D. Blanco, H. Casini, L.-Y. Hung, and R. C. Myers, Relative Entropy and Holography, *JHEP* **08**, 060, arXiv:1305.3182 [hep-th].

[58] C. P. Herzog and K.-W. Huang, Stress Tensors from Trace Anomalies in Conformal Field Theories, *Phys. Rev. D* **87**, 081901 (2013), arXiv:1301.5002 [hep-th].

[59] T. Jacobson, Black hole entanglement entropy and the renormalization group, *Phys. Rev. D* **87**, 084047 (2013), arXiv:1212.6824 [hep-th].

[60] A. C. Wall, A Survey of Black Hole Thermodynamics (2018), arXiv preprint, arXiv:1804.10610 [gr-qc].

[61] D. Brout, D. Scolnic, B. Popovic, A. G. Riess, J. Zuntz, R. Kessler, A. Carr, T. M. Davis, S. Hinton, D. O. Jones, W. D. Kenworthy, E. R. Peterson, K. Said, and et al., The pantheon+ analysis: Cosmological constraints, *Astrophysical Journal* **938**, 110 (2022), arXiv:2202.04077 [astro-ph.CO].

[62] C. Zhang, H. Zhang, S. Yuan, S. Liu, T.-J. Zhang, and Y.-C. Sun, Four new observational h(z) data from luminous red galaxies in the Sloan Digital Sky Survey data release seven, *Research in Astronomy and Astrophysics* **14**, 1221 (2014), arXiv:1207.4541 [astro-ph.CO].

[63] J. Simon, L. Verde, and R. Jimenez, Constraints on the redshift dependence of the dark energy potential, *Phys. Rev. D* **71**, 123001 (2005).

[64] M. Moresco *et al.*, Improved constraints on the expansion rate of the universe up to $z \sim 1.1$ from the spectroscopic evolution of cosmic chronometers, *Journal of Cosmology and Astroparticle Physics* **2012** (08), 006.

[65] M. Moresco *et al.*, A 6% measurement of the hubble parameter at $z \sim 0.45$: direct evidence of the epoch of cosmic re-acceleration, *Journal of Cosmology and Astroparticle Physics* **2016** (05), 014.

[66] M. Moresco, Raising the bar: new constraints on the hubble parameter with cosmic chronometers at $z \sim 2$, *Monthly Notices of the Royal Astronomical Society: Letters* **450**, L16 (2015).

[67] A. L. Ratsimbazafy, S. I. Loubser, S. M. Crawford, C. M. Cress, B. A. Bassett, R. C. Nichol, and P. Väistönen, Age-dating luminous red galaxies observed with the southern african large telescope, *Monthly Notices of the Royal Astronomical Society* **467**, 3239 (2017).

[68] D. Stern, R. Jimenez, L. Verde, M. Kamionkowski, and S. A. Stanford, Cosmic chronometers: constraining the equation of state of dark energy. i: $H(z)$ measurements, *Journal of Cosmology and Astroparticle Physics* **2010** (02), 008.

[69] A. G. Sanchez *et al.* (BOSS), The clustering of galaxies in the SDSS-III Baryon Oscillation Spectroscopic Survey: cosmological implications of the full shape of the clustering wedges in the data release 10 and 11 galaxy samples, *Mon. Not. Roy. Astron. Soc.* **440**, 2692 (2014), arXiv:1312.4854 [astro-ph.CO].

[70] H. Gil-Marín, W. J. Percival, L. Verde, J. R. Brownstein, C.-H. Chuang, F.-S. Kitaura, S. A. Rodríguez-Torres, and M. D. Olmstead, The clustering of galaxies in the SDSS-III Baryon Oscillation Spectroscopic Survey: RSD measurement from the power spectrum and bispectrum of the DR12 BOSS galaxies, *Mon. Not. Roy. Astron. Soc.* **465**, 1757 (2017), arXiv:1606.00439 [astro-ph.CO].

[71] C.-H. Chuang *et al.* (BOSS), The clustering of galaxies in the SDSS-III Baryon Oscillation Spectroscopic Survey: single-probe measurements from CMASS anisotropic galaxy clustering, *Mon. Not. Roy. Astron. Soc.* **461**, 3781 (2016), arXiv:1312.4889 [astro-ph.CO].

[72] F. Beutler *et al.* (BOSS), The clustering of galaxies in the completed SDSS-III Baryon Oscillation Spectroscopic Survey: Anisotropic galaxy clustering in Fourier-space, *Mon. Not. Roy. Astron. Soc.* **466**, 2242 (2017), arXiv:1607.03150 [astro-ph.CO].

[73] Y. Wang, G.-B. Zhao, C.-H. Chuang, M. Pellejero-Ibanez, C. Zhao, F.-S. Kitaura, and S. Rodriguez-Torres, The clustering of galaxies in the completed SDSS-III Baryon Oscillation Spectroscopic Survey: a tomographic analysis of structure growth and expansion rate from anisotropic galaxy clustering, *Mon. Not. Roy. Astron. Soc.* **481**, 3160 (2018), arXiv:1709.05173 [astro-ph.CO].

[74] R. Tojeiro *et al.* (BOSS), The clustering of galaxies in the SDSS-III Baryon Oscillation Spectroscopic Survey: measuring structure growth using passive galaxies, *Mon. Not. Roy. Astron. Soc.* **424**, 2339 (2012), arXiv:1203.6565 [astro-ph.CO].

[75] C. Blake *et al.*, The WiggleZ Dark Energy Survey: Joint measurements of the expansion and growth history at $z < 1$, *Mon. Not. Roy. Astron. Soc.* **425**, 405 (2012), arXiv:1204.3674 [astro-ph.CO].

[76] S. de la Torre *et al.*, The VIMOS Public Extragalactic Redshift Survey (VIPERS). Galaxy clustering and redshift-space distortions at $z=0.8$ in the first data release, *Astron. Astrophys.* **557**, A54 (2013), arXiv:1303.2622 [astro-ph.CO].

[77] M. J. Wilson, *Geometric and growth rate tests of General Relativity with recovered linear cosmological perturbations*, Ph.D. thesis, Edinburgh U. (2017), arXiv:1610.08362 [astro-ph.CO].

[78] A. J. Hawken *et al.*, The VIMOS Public Extragalactic Redshift Survey: Measuring the growth rate of structure around cosmic voids, *Astron. Astrophys.* **607**, A54 (2017), arXiv:1611.07046 [astro-ph.CO].

[79] S. de la Torre *et al.*, The VIMOS Public Extragalactic Redshift Survey (VIPERS). Gravity test from the combination of redshift-space distortions and galaxy-galaxy lensing at $0.5 < z < 1.2$, *Astron. Astrophys.* **608**, A44 (2017), arXiv:1612.05647 [astro-ph.CO].

[80] A. Pezzotta *et al.*, The VIMOS Public Extragalactic Redshift Survey (VIPERS): The growth of structure at $0.5 < z < 1.2$ from redshift-space distortions in the clustering of the PDR-2 final sample, *Astron. Astrophys.* **604**, A33 (2017), arXiv:1612.05645 [astro-ph.CO].

[81] F. G. Mohammad *et al.*, The VIMOS Public Extragalactic Redshift Survey (VIPERS). An unbiased estimate of the growth rate of structure at $\langle z \rangle = 0.85$ using the clustering of luminous blue galaxies, *Astron. Astrophys.* **610**, A59 (2018), arXiv:1708.00026 [astro-ph.CO].

[82] C. Howlett, L. Staveley-Smith, P. J. Elahi, T. Hong, T. H. Jarrett, D. H. Jones, B. S. Koribalski, L. M. Macri, K. L. Masters, and C. M. Springob, 2MTF – VI. Measuring the velocity power spectrum, *Mon. Not. Roy. Astron. Soc.* **471**, 3135 (2017), arXiv:1706.05130 [astro-ph.CO].

[83] M. Davis, A. Nusser, K. Masters, C. Springob, J. P. Huchra, and G. Lemson, Local Gravity versus Local Velocity: Solutions for β and nonlinear bias, *Mon. Not. Roy. Astron. Soc.* **413**, 2906 (2011), arXiv:1011.3114 [astro-ph.CO].

[84] M. J. Hudson and S. J. Turnbull, The growth rate of cosmic structure from peculiar velocities at low and high redshifts, *Astrophys. J. Lett.* **751**, L30 (2013), arXiv:1203.4814 [astro-ph.CO].

[85] F. Beutler, C. Blake, M. Colless, D. H. Jones, L. Staveley-Smith, G. B. Poole, L. Campbell, Q. Parker, W. Saunders, and F. Watson, The 6dF Galaxy Survey: $z \approx 0$ measurement of the growth rate and σ_8 , *Mon. Not. Roy. Astron. Soc.* **423**, 3430 (2012), arXiv:1204.4725 [astro-ph.CO].

[86] D. Huterer, D. Shafer, D. Scolnic, and F. Schmidt, Testing Λ CDM at the lowest redshifts with SN Ia and galaxy velocities, *JCAP* **05**, 015, arXiv:1611.09862 [astro-ph.CO].

[87] T. Okumura *et al.*, The Subaru FMOS galaxy redshift survey (FastSound). IV. New constraint on gravity theory from redshift space distortions at $z \sim 1.4$, *Publ. Astron. Soc. Jap.* **68**, 38 (2016), arXiv:1511.08083 [astro-ph.CO].

[88] G.-B. Zhao *et al.* (eBOSS), The clustering of the SDSS-IV extended Baryon Oscillation Spectroscopic Survey DR14 quasar sample: a tomographic measurement of cosmic structure growth and expansion rate based on optimal redshift weights, *Mon. Not. Roy. Astron. Soc.* **482**, 3497 (2019), arXiv:1801.03043 [astro-ph.CO].

[89] H. Gil-Marín *et al.* (eBOSS), The clustering of the SDSS-IV extended Baryon Oscillation Spectroscopic Survey DR14 quasar sample: structure growth rate measurement from the anisotropic quasar power spectrum in the redshift range $0.8 < z < 2.2$, *Mon. Not. Roy. Astron. Soc.* **477**, 1604 (2018), arXiv:1801.02689 [astro-ph.CO].

[90] J. Hou *et al.* (eBOSS), The clustering of the SDSS-IV extended Baryon Oscillation Spectroscopic Survey DR14 quasar sample: anisotropic clustering analysis in configuration-space, *Mon. Not. Roy. Astron. Soc.* **480**, 2521 (2018), arXiv:1801.02656 [astro-ph.CO].

[91] L. Kazantzidis and L. Perivolaropoulos, Evolution of the $f\sigma_8$ tension with the Planck15/ΛCDM determination and implications for modified gravity theories, *Phys. Rev. D* **97**, 103503 (2018), arXiv:1803.01337 [astro-ph.CO].

[92] Y.-S. Song and W. J. Percival, Reconstructing the history of structure formation using Redshift Distortions, *JCAP* **10**,

004, arXiv:0807.0810 [astro-ph].

[93] L. Samushia, W. J. Percival, and A. Raccanelli, Interpreting large-scale redshift-space distortion measurements, *Mon. Not. Roy. Astron. Soc.* **420**, 2102 (2012), arXiv:1102.1014 [astro-ph.CO].

[94] C.-H. Chuang and Y. Wang, Modeling the Anisotropic Two-Point Galaxy Correlation Function on Small Scales and Improved Measurements of $H(z)$, $D_A(z)$, and $\beta(z)$ from the Sloan Digital Sky Survey DR7 Luminous Red Galaxies, *Mon. Not. Roy. Astron. Soc.* **435**, 255 (2013), arXiv:1209.0210 [astro-ph.CO].

[95] C. Howlett, A. Ross, L. Samushia, W. Percival, and M. Manera, The clustering of the SDSS main galaxy sample – II. Mock galaxy catalogues and a measurement of the growth of structure from redshift space distortions at $z = 0.15$, *Mon. Not. Roy. Astron. Soc.* **449**, 848 (2015), arXiv:1409.3238 [astro-ph.CO].

[96] M. Feix, A. Nusser, and E. Branchini, Growth Rate of Cosmological Perturbations at $z \sim 0.1$ from a New Observational Test, *Phys. Rev. Lett.* **115**, 011301 (2015), arXiv:1503.05945 [astro-ph.CO].

[97] M. Feix, E. Branchini, and A. Nusser, Speed from light: growth rate and bulk flow at $z \sim 0.1$ from improved SDSS DR13 photometry, *Mon. Not. Roy. Astron. Soc.* **468**, 1420 (2017), arXiv:1612.07809 [astro-ph.CO].

[98] C. Blake *et al.*, Galaxy And Mass Assembly (GAMA): improved cosmic growth measurements using multiple tracers of large-scale structure, *Mon. Not. Roy. Astron. Soc.* **436**, 3089 (2013), arXiv:1309.5556 [astro-ph.CO].

[99] F. Shi *et al.*, Mapping the Real Space Distributions of Galaxies in SDSS DR7: II. Measuring the growth rate, clustering amplitude of matter and biases of galaxies at redshift 0.1, *Astrophys. J.* **861**, 137 (2018), arXiv:1712.04163 [astro-ph.CO].

[100] D. Foreman-Mackey, D. W. Hogg, D. Lang, and J. Goodman, emcee: The MCMC Hammer, *Publ. Astron. Soc. Pac.* **125**, 306 (2013), arXiv:1202.3665 [astro-ph.IM].

[101] A. Lewis, GetDist: a Python package for analysing Monte Carlo samples, *JCAP* **08**, 025, arXiv:1910.13970 [astro-ph.IM].

[102] M. Asgari *et al.*, Kids-1000 cosmology: Cosmic shear constraints and comparison between two-point statistics, *Astronomy & Astrophysics* **645**, A104 (2021), arXiv:2007.15633 [astro-ph.CO].

[103] C. Heymans *et al.*, Kids-1000 cosmology: Multi-probe weak gravitational lensing and spectroscopic galaxy clustering constraints, *Astronomy & Astrophysics* (2021), arXiv:2007.15632 [astro-ph.CO].

[104] L. F. Secco, S. Samuroff, E. Krause, B. Jain, J. Blazek, *et al.*, Dark energy survey year 3 results: Cosmology from cosmic shear and robustness to modeling uncertainty, *Physical Review D* (2022), arXiv:2105.13544 [astro-ph.CO].

[105] J. H. Cooperman and M. A. Luty, Renormalization of entanglement entropy and the gravitational effective action, *JHEP* **12**, 045, arXiv:1302.1878 [hep-th].

[106] SDSS-IV Collaboration, Final bao and rsd measurements, <https://www.sdss4.org/science/final-bao-and-rsd-measurements/>, accessed: 2025-10-23.

[107] S. J. Turnbull, M. J. Hudson, H. A. Feldman, M. Hicken, R. P. Kirshner, and R. Watkins, Cosmic flows in the nearby universe from Type Ia Supernovae, *Mon. Not. Roy. Astron. Soc.* **420**, 447 (2012), arXiv:1111.0631 [astro-ph.CO].